Probing Interstellar Grain Growth Through Polarimetry in the Taurus Cloud Complex

John E. Vaillancourt,[1,2] B-G Andersson,[2] Dan P. Clemens,[3] Vilppu Piirola,[4] Thiem Hoang,[5] Eric E. Becklin,[2,6] and Miranda Caputo[2,7]

[1]*Lincoln Laboratory, Massachusetts Institute of Technology, 244 Wood St., Lexington, MA 02421-6426*
[2]*SOFIA Science Center, Universities Space Research Association, NASA Ames Research Center, Moffett Field, CA 94035*
[3]*Institute for Astrophysical Research and Department of Astronomy, Boston University, 725 Commonwealth Ave., Boston, MA 02215*
[4]*Tuorla Observatory, University of Turku, FI-21500 Piikkiö, Finland*
[5]*Korean Astronomy and Space Science Institute, Daejeon 34055, Korea, and Korean University of Science and Technology, Daejeon, 34113, Korea*
[6]*Department of Physics & Astronomy, University of California, Los Angeles*
[7]*Ritter Astrophysical Research Center, University of Toledo Dept. of Physics and Astronomy, 2801 W. Bancroft St. Toledo, Ohio 43606*

ABSTRACT

The optical and near-infrared (OIR) polarization of starlight is typically understood to arise from the dichroic extinction of that light by dust grains whose axes are aligned with respect to a local magnetic field. The size distribution of the aligned grain population can be constrained by measurements of the wavelength dependence of the polarization. The leading physical model for producing the alignment is that of radiative alignment torques (RAT), which predicts that the most efficiently aligned grains are those with sizes larger than the wavelengths of light composing the local radiation field. Therefore, for a given grain size distribution, the wavelength at which the polarization reaches a maximum (λ_{max}) should correlate with the characteristic reddening along the line of sight between the dust grains and the illumination source. A correlation between λ_{max} and reddening has been previously established for extinctions up to $A_V \approx 4$ mag. We extend the study of this relationship to a larger sample of stars in the Taurus cloud complex, including extinctions $A_V > 10$ mag. We confirm the earlier results for $A_V < 4$ mag, but find that the λ_{max} vs. A_V relationship bifurcates above $A_V \approx 4$ mag, with part of the sample continuing the previously observed relationship. The remaining sample exhibits a steeper rise in λ_{max} vs. A_V. We propose that the data exhibiting the steep rise represent lines of sight of high-density "clumps", where grain coagulation has taken place. We present RAT-based modeling supporting these hypotheses. These results indicate that multi-band OIR polarimetry is a powerful tool for tracing grain growth in molecular clouds, independent of uncertainties in the dust temperature and emissivity.

Keywords: Astrophysical dust processes (99), Interstellar dust (836), Interstellar medium (847), Polarimetry (1278), Starlight polarization (1571), Spectropolarimetry (1973)

1. INTRODUCTION

Starlight passing through the interstellar medium (ISM) is typically polarized at the level of a few percent. The upper envelope of the polarization fraction correlates well with the extinction (e.g., Hiltner 1949a; Serkowski 1968; Fosalba et al. 2002), and the position angle is in good agreement with independent measurements of the interstellar magnetic-field orientation (e.g., Spoelstra 1984; Scarrott et al. 1987; Page et al. 2007). Thus, the observed optical and near-infrared (OIR) polarization, and the complementary far-infrared polarized emission (e.g., Cudlip et al. 1982; Dotson et al. 2000), have long been attributed to asymmetric dust grains aligned with the interstellar magnetic field (e.g., Hiltner 1949b; Hildebrand 1988). Polarimetry can provide a powerful tool for probing interstellar magnetic fields (Davis 1951; Chandrasekhar & Fermi 1953) if the process of dust grain alignment can be understood.

Attempts to explain grain alignment began with its discovery (Hiltner 1949a; Hall 1949) and included ferromagnetic alignment (Spitzer & Tukey 1949), mechanical alignment (Gold 1952), and paramagnetic relaxation (Davis & Greenstein 1951). Significant progress has been achieved in the last decade, both theoretically and observationally (see reviews by Lazarian et al. 2015; Andersson 2015; Andersson et al. 2015). New calculations (Lazarian & Draine 1999; Hoang & Lazarian 2016) and observations (Hough et al. 2008) have shown that paramagnetic relaxation (or its modifications—Purcell 1976; Mathis 1986) likely cannot provide an explanation of the observed interstellar polarization. In contrast, a quantitative theory based on direct radiative alignment torques (RATs; e.g., Draine & Weingartner 1996, 1997) now provides specific testable predictions (Lazarian & Hoang 2007; Hoang & Lazarian 2008). The aim of this work is to extend tests of the prediction that the alignment efficiency depends on the color of the local radiation field and the size distribution of the grains.

The basic requirement for grain alignment in RAT theory is that a grain of effective radius a, with net helicity, be exposed to an anisotropic radiation field with a wavelength λ that is less than the grain diameter (Lazarian & Hoang 2007). Grain he-

licity is satisfied for any irregularly shaped grain. Radiation fields in the ISM are almost always anisotropic since the grain is either located close to a discrete radiation source (star) and/or the interstellar cloud in which it is embedded has a well defined density gradient and hence a net radiation-flow vector. The size constraint follows in a manner similar to Mie scattering theory (e.g., Martin 1974) such that the coupling of the aligning radiation to the grains drops rapidly for $\lambda > 2a$ (Lazarian & Hoang 2007)[1]. From these requirements, it follows that the color and intensity of the radiation field are key factors in radiative grain alignment. Support of this dependence comes from observations of correlations between radiation field strengths and polarization (Whittet et al. 2008; Medan & Andersson 2019)

Tests of the RAT predictions require measurements that trace grain alignment efficiency, preferably as a function of grain size. The fractional polarization p/τ (where τ is the optical depth at some chosen wavelength) nominally traces the alignment (Whittet et al. 2008), but is not directly sensitive to changes in the grain size distribution and cannot be used to distinguish between line of sight alignment variations and changes in magnetic field structure and turbulence (Jones 1989).

A better measure of the size distribution of aligned grains is the wavelength dependence of the polarization because relative variations in this spectrum are independent of the grain alignment orientation with respect to the line of sight. Empirically, the wavelength dependence of interstellar polarization is parameterized by the wavelength at which the polarization peaks, $\lambda_{\max}$, using the function

$$\frac{p(\lambda)}{p_{\max}} = \exp\left[-K \ln^2\left(\frac{\lambda}{\lambda_{\max}}\right)\right], \qquad (1)$$

referred to as the "Serkowski relation" (Serkowski et al. 1975) if the parameter K is set to the fixed value 1.15, or the "Wilking relation" (Wilking et al. 1980) if K is used as a fitting parameter.

Kim & Martin (1995) showed theoretically that $\lambda_{\max}$ depends on the average size of aligned grains, and is especially sensitive to the size of the smallest grains in the distribution. By inverting the observed extinction and polarization curves, they showed, in agreement with earlier studies (Mathis et al. 1977), that the overall dust size distribution extends to very small grains ($a \sim 0.01\,\mu$m), but that the aligned silicate grains in the diffuse ISM typically do not have sizes smaller than $a = 0.04$–$0.05\,\mu$m. Since interstellar extinction increases as the wavelength of incident radiation becomes bluer, RAT alignment predicts that the size of the smallest aligned grain will increase as the radiation is reddened into the cloud—hence $\lambda_{\max}$ should be correlated with the extinction A_V.

Using multi-band polarimetry, Whittet et al. (2001) noted a weak correlation between $\lambda_{\max}$ and A_V in their Taurus sample. Andersson & Potter (2007) re-analyzed those data and showed that, if several observational biases are taken into account (most importantly line of sight where the visual extinc-

tion and the FIR color temperatures were inconsistent), this correlation becomes well defined and is present for all six nearby interstellar clouds probed in their study. However, the observational samples analyzed in Andersson & Potter (2007) were of limited size and only covered the extinction range up to $A_V \sim 4$ mag, with the exception of a very small number of higher extinction data points. For the Taurus cloud, Andersson & Potter (2007) found

$$\lambda_{\max} = (0.53 \pm 0.01\ \mu\text{m}) + (0.020 \pm 0.004\ \mu\text{m}\,\text{mag}^{-1})A_V. \quad (2)$$

If the RAT prediction is correct (that the minimum aligned-grain size will increase as the radiation is reddened), and the grain size distribution is constant, then this $\lambda_{\max}$-A_V relation should continue to higher levels of extinction, where very few targets have been previously observed. To date, the location of the peak polarization towards one star, Elias 3-16 at $A_V = 24.1 \pm 0.1$ mag (Murakawa et al. 2000) and $\lambda_{\max} = 1.08 \pm 0.08\,\mu$m (Hough et al. 1988), is consistent with the linear relation in equation (2).

Our goal here is to test the low-extinction results found by Whittet et al. (2001) and Andersson & Potter (2007) and determine if the $\lambda_{\max}$-A_V trend continues at $A_V > 4$ mag. We have chosen to focus on the Taurus cloud complex as it is well studied in many tracers and covers a wide range of extinctions (see Kenyon et al. (2008) for a review). Of particular importance for our purposes, Taurus, being near-by, has background field-stars that tend to be reasonably bright and therefore amenable to high quality polarimetry. Several authors have surveyed the cloud in polarimetry (Whittet 1992; Whittet et al. 2008, and refs therein) and near infrared photometry (e.g. Shenoy et al. 2008)

We present two additional data sets for stars in the Taurus cloud complex not previously observed in polarization at multiple wavelengths. Our target stars have been selected to be true background stars (behind the cloud complex from our LOS), thereby avoiding the complications of grain alignment variations induced in the circumstellar environment of embedded stars (Whittet et al. 2008). These new observations are described in Section 2. Section 3 presents fits to the Serkowski and Wilking relations for these new data sets and includes discussion of the results of some individual stars. Within Sections 2–3 there are three tables for each of the two data sets: 1) Tables 1 and 2 contain lists of the observed stars along with characteristics such as apparent brightness, extinction, and distance; 2) Tables 3 and 4 contain the Stokes parameters fitted to the polarization data for each star and each bandpass; and 3) Tables 5 and 6 contain fits to the Serkowski and Wilking relations for each star. Section 4 examines the $\lambda_{\max}$-A_V relation and its variations and uses an RAT grain-alignment model to interpret the observational results. Our results and conclusions are summarized in Section 5.

2. OBSERVATIONS & DATA REDUCTION

2.1. *Target Selection*

Our sample of low-extinction stars (Table 1) was based on the Wright et al. (2003) survey of spectroscopically-classified

---

[1] The radiative torque efficiency does not fully disappear at $\lambda > 2a$, but drops as $(\lambda/a)^{-\alpha}$, with $\alpha \sim 3$–4.
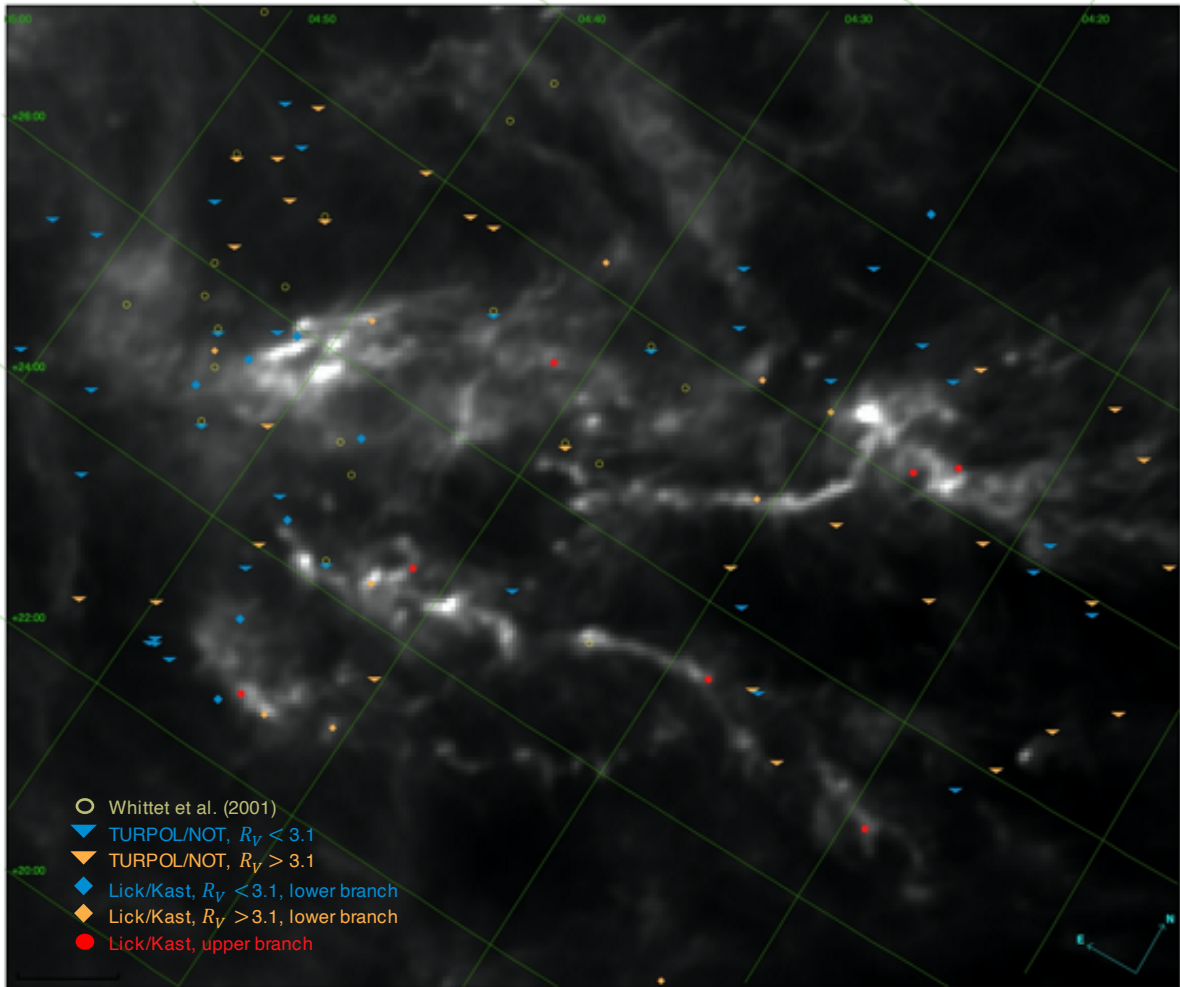
Figure 1. Location of the stars observed in polarization in the Taurus Cloud Complex, plotted on the *Planck* $350\,\mu$m map (Planck Collaboration et al. 2018). Stars in the sample of Whittet et al. (2001) are shown as yellow circles. Stars observed by NOT/TURPOL are shown as triangles (blue and orange) and stars observed with Lick/Kast on the "lower branch" of the $\lambda_{\max}$-A_V relation (Section 4.1) are shown as diamonds (blue and orange). In both data sets, stars with $R_V < 3.1$ are blue and stars with $R_V > 3.1$ are orange. Red circles are Lick/Kast targets on the "upper branch" of the $\lambda_{\max}$-A_V relation (Section 4.1).

Tycho targets (Høg et al. 2000), screening out sightlines with anomalous visual extinctions, following the procedure in Andersson & Potter (2007). As described in that paper, such anomalous lines of sight represent material where, based on comparisons of A_V and FIR dust color-temperature, the line-of-sight visual extinction (A_V) does not accurately represent the effective radiation field seen by the dust. This can be due to the geometry of the cloud or the presence of near-by discrete radiation sources. We selected stars from two fields of 3 degree radius centered at Right Ascension, Declination (J2000): ($4^\mathrm{h}15^\mathrm{m}$, $28°0'$) and ($4^\mathrm{h}40^\mathrm{m}$, $25°30'$). Using Tycho and 2MASS (Skrutskie et al. 2006) photometry, we derived visual extinctions (A_V) and the total-to-selective-extinction ratio (R_V).

The high-extinction stellar sample list was generated using stars from the surveys by Teixeira & Emerson (1999), Murakawa et al. (2000), and Shenoy et al. (2008, hereafter SWIW) (Table 2). We screened these for embedded sources by rejecting any targets that show associated flux in the 60 or $100\,\mu$m

bands of IRAS. At the time of the observations, NOMAD[2] photometry was available for most stars at B-, V-, and R-bands, as is 2MASS photometry at J-, H-, and K_s-bands. Because of the marginal photometric accuracy of the NOMAD data, the visual extinctions are, where available, taken from SWIW, and are based on the relation $A_V = (5.3 \pm 0.3) \times E_{J-K}$ (c.f., SWIW). The selected sample contains the 25 stars listed in Table 2 and spans extinctions from $A_V = 3$ to 10 magnitudes (Figure 2).

In order to sample the material in the cloud we also limit the stellar sample to those stars behind the cloud. Distances from the Gaia DR2 parallax survey (Gaia Collaboration et al. 2018) are shown in Tables 1 and 2, and discussed further in Section 3.3. Figure 1 shows the location of all stars in our sample within the structure of the Taurus Cloud Complex, which is traced by the total dust emission at $160\,\mu$m. (The stars are

---

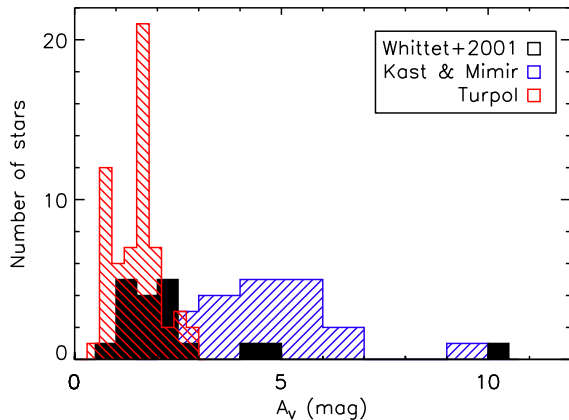[2] http://www.usno.navy.mil/USNO/astrometry/optical-IR-prod/nomad

Figure 2. Distribution of extinctions. The number of stars in several extinction bins for the work of Whittet et al. (2001), as well as the data presented in this work obtained using the Kast (Section 2.3), Mimir (Section 2.4), and Turpol (Section 2.2) instruments. The Turpol data cover an extinction range similar to that of the Whittet et al. data, while the Kast and Mimir data extend the data sets to higher extinction levels.

plotted as different colors based on R_V and the λ_{max}-A_V relation discussed in Section 4.1.)

2.2. *Optical Photo-polarimetry*

We used the TurPol instrument on the 2.5 m Nordic Optical Telescope (NOT) at Roque de los Muchachos Observatory on La Palma, during the nights of 2007 November 3–6, to perform broad-band multicolor polarimetry of stars background to the Taurus molecular cloud. The instrument provides simultaneous measurements in five passbands close to the *UBVRI* system, by using four dichroic filters to split the light into the different spectral regions (Piirola 1988). The instrument was used in linear polarimetry mode. The half-wave plate (HWP) was rotated in 22.5 degree steps, with one complete observation of linear polarization consisting of eight integrations. Standard stars were observed each night to calibrate the position angle zero-point and determine the instrumental polarization.

2.3. *Optical Spectropolarimetry*

We performed spectropolarimetric observations of high-extinction lines of sight using the red-channel (0.4–1.1 μm) of the Kast spectropolarimeter (Miller, Robinson, & Goodrich 1988) on the 3 m Shane telescope of Lick Observatory during the nights of 2009 November 15–17 (UT). The incident polarization was modulated by rotating a HWP through eight 22.5 degree steps, spanning the range 0–157.5 degrees, and integrating for 20–60 seconds per step, depending on the stellar brightness. Spectra in both orthogonal modes of linear polarization were simultaneously imaged onto a 1200×400 pixel CCD with 27 μm pixels (manufactured by EG&G Reticon; Cizdziel 1990). Typical observations used wide slits ($3''–5''$) yielding stellar images of ~4 camera pixels full-width at half maxium (FWHM). In conjunction with a 300 lines per millimeter grating, at a blaze angle corresponding to 7500 Å, the resulting spectra have resolutions of ≈20 Å (FWHM).

Detailed discussion of the stellar polarization data analyses are presented in Appendix A along with calibration results and procedures in Appendix B. Wavelength calibration was achieved by regularly observing arc lamps composed of argon, helium, and neon. Flat-field corrections utilized dome flats, separately normalizing the two orthogonal polarization components in each image and for each of the eight HWP angles. Two unpolarized standard stars were used to measure the level of instrument polarization and four high-polarization standard stars to calibrate the polarization position angle. Additionally, the unpolarized standards were used in conjunction with a polarizing filter in order to characterize the wavelength dependence of the polarization efficiency and offset angles of the HWP.

Spectral classification of the spectro-polarimetry sample stars was accomplished by comparing the Stokes *I* spectra with the standard sequence from Jacoby et al. (1984) and other classification estimates in the literature (e.g. Murakawa et al. 2000). The spectral classification was performed independently by two astronomers whose separate spectral class estimates agreed to within 1–2 subclasses. Given the limited spectral resolution (20 Å), reliable luminosity class determinations are not possible and we have, therefore, assigned luminosity class V (Main Sequence) to all stars earlier than G0 and class III (Giant) to later spectral types. Using parallaxes, archival photometry, and absolute magnitudes measured by Gaia (Gaia Collaboration et al. 2018) we found that this assumption held true for all stars in our sample except for SWIW 040, SWIW 148, and Tamura 17.

2.4. *Near-Infrared Polarimetry*

Imaging polarimetric observations in the near-infrared (NIR) *H*-band (1.63 μm) took place on the nights of 2011 September 18 and 19 and again on 2012 January 11 using the Mimir instrument (Clemens et al. 2007) on the 1.83 m Perkins telescope, located outside Flagstaff, AZ. Mimir used a rotating compound HWP, an MKO *H*-band filter, a PK50 long-wave blocker, and a fixed wire-grid to perform step-and-integrate polarimetry over a $10' \times 10'$ field of view at 0.6 arcsec per pixel onto a 1024^2 pixel Aladdin III InSb detector array. A single observation sequence consisted of pointing the telescope to each of six sky dither positions, located about a 15 arcsec wide hexagon, and collecting 16 images, each through HWP orientations offset by 22.5°, to sample one complete turn of the HWP. This yielded four independent sets of Stokes *q* and *u*. In-dome calibrations included linearity, polarization flat-fields, and dark current images. Sky calibrations consisted of observations of fields containing multiple polarization standard stars. Further detail of the data collection steps, data processing and polarimetric extractions are to be found in Clemens et al. (2012a,b).

Some of the stars in Table 2 are the brightest observed for polarimetry by Mimir and some of the 2011 observations had poorly matched exposure times. The 2012 observations used reduced integration times (0.25–1.75 seconds vs. 0.65–3.25 seconds per exposure), yielding lower uncertainties. For the non-saturated stars observed in both runs, variance-weighted averaging of Stokes *q* and *u* was performed and prop-

agated into polarization percentages and equatorial position angles and their associated uncertainties. Single observations of bright stars are limited to about 0.15%–0.2% polarization percentage uncertainty and about 1°–2° position angle uncertainty.

Table 1. TurPol Sources

Star	RA (J2000) (hh:mm:ss.s)	Dec. (J2000) (dd:mm:ss.s)	V^a (mag.)	R_V	σ_{R_V}	A_V (mag.)	σ_{A_V} (mag.)
PPM 93181	4:02:15.2	27:10:36.7	9.8	6.24	2.61	0.74	0.08
PPM 93195	4:03:38.8	28:39:42.3	8.1	4.10	0.64	1.09	0.09
PPM 93213	4:04:22.4	26:42:12.8	10.8	6.41	5.33	0.85	0.14
PPM 93236	4:05:28.8	27:52:46.7	8.4	2.24	0.32	0.80	0.08
PPM 92238	4:05:36.1	26:05:18.8	10.5	4.37	1.01	0.88	0.08
PPM 93241	4:05:44.7	27:58:47.7	10.6	3.30	1.67	0.60	0.12
PPM 93260	4:06:41.4	25:43:19.7	8.0	2.94	0.67	0.58	0.08
PPM 93265	4:07:05.1	29:26:25.9	10.0	4.87	0.56	2.71	0.09
PPM 93280	4:08:40.8	28:14:56.4	10.6	2.57	0.39	2.23	0.11
PPM 93281	4:08:41.3	27:56:40.0	10.8	2.64	0.79	1.02	0.11
PPM 93289	4:09:21.1	29:43:47.4	9.9	3.51	0.55	1.59	0.09
BD+27645	4:11:16.4	27:55:45.0	10.1	6.07	2.59	1.02	0.09
PPM 93320	4:11:57.1	27:10:05.9	10.3	3.31	1.12	0.66	0.10
BD+24636	4:13:53.5	25:02:09.5	10.4	2.75	0.39	1.43	0.09
PPM 93369	4:15:24.6	29:21:57.1	10.2	4.11	0.59	2.05	0.14
PPM 93376	4:16:10.2	25:31:04.6	9.4	3.50	0.35	1.93	0.10
PPM 93377	4:16:11.1	29:07:15.4	9.7	2.93	0.27	1.98	0.09
BD+25689	4:16:26.0	25:30:42.9	11.2	3.27	0.96	1.80	0.15
PPM 93390	4:17:13.3	27:19:44.5	11.1	6.70	2.34	2.01	0.12
PPM 93403	4:18:14.8	29:16:06.1	10.4	3.54	0.56	1.78	0.10
BD+25698	4:18:46.2	26:08:57.1	9.2	2.74	0.29	1.36	0.08
HD 283581	4:20:07.4	26:24:40.5	11.4	2.31	1.26	0.70	0.16
HD 283569	4:20:48.3	28:29:39.6	11.2	2.32	0.52	1.52	0.13
PPM 93449	4:21:55.7	29:39:01.0	8.5	3.28	0.37	1.30	0.08
PPM 93510	4:25:33.0	28:26:58.1	10.5	1.62	0.40	0.77	0.08
HD 283625	4:26:51.6	28:57:11.1	11.4	2.95	0.92	1.71	0.15
HD 28170	4:27:34.0	25:03:41.7	9.0	3.30	0.32	1.62	0.08
PPM 93537	4:28:17.9	27:46:50.5	7.8	2.99	0.26	1.49	0.08
PPM 93546	4:29:02.9	26:30:58.9	10.8	2.38	0.38	1.65	0.11
HD 28482	4:30:22.4	23:35:19.9	7.2	3.87	0.50	1.67	0.14
HD 28975	4:34:50.2	24:14:40.3	9.0	3.22	0.28	1.72	0.07
BD+26728	4:34:55.0	27:12:11.3	9.6	2.92	0.25	2.68	0.14
PPM 93637	4:37:09.1	27:55:32.7	7.5	3.55	0.76	0.68	0.08

Table 1 *continued*

Table 1 (*continued*)

Star	RA (J2000) (hh:mm:ss.s)	Dec. (J2000) (dd:mm:ss.s)	V^a (mag.)	R_V	σ_{R_V}	A_V (mag.)	σ_{A_V} (mag.)
PPM 93641	4:37:38.9	23:46:56.5	10.0	3.12	0.81	0.89	0.06
PPM 93642	4:37:46.3	24:02:45.9	9.7	3.19	0.38	1.56	0.09
PPM 93644	4:38:06.6	22:37:25.8	9.9	3.24	0.76	0.81	0.08
HD 29334	4:38:09.8	24:33:13.3	9.1	3.80	0.41	1.56	0.07
BD+27675	4:38:15.2	27:52:50.7	10.7	3.34	0.81	1.18	0.09
BD+22723	4:39:00.2	22:40:13.8	10.5	2.68	0.55	1.03	0.10
PPM 93658	4:39:06.7	22:42:43.4	9.8	2.90	0.47	0.97	0.09
PPM 93660	4:39:13.5	22:39:08.1	8.6	3.63	1.00	0.77	0.14
PPM 93668	4:39:59.1	23:00:52.5	8.8	4.33	0.47	1.67	0.08
PPM 93675	4:40:21.0	25:03:07.7	9.8	5.76	1.27	1.54	0.08
HD 283772	4:40:59.3	27:59:25.5	10.6	3.10	0.52	1.88	0.15
BD+25724	4:42:19.9	25:51:48.3	10.8	3.76	0.56	2.61	0.12
PPM 93713	4:42:41.2	24:41:17.9	10.0	4.30	0.40	2.63	0.09
BD+22741	4:42:44.0	22:36:19.4	10.9	6.29	2.41	1.55	0.12
PPM 93722	4:43:27.3	27:01:37.0	9.8	3.99	0.68	1.57	0.14
BD+25727	4:44:24.9	25:31:42.7	9.5	3.20	0.28	2.12	0.09
BD+26742	4:45:14.0	27:00:07.4	10.0	5.50	1.17	2.02	0.11
HD 30122	4:45:42.5	23:37:40.8	6.3	3.25	0.59	0.74	0.08
BD+26746	4:46:02.8	26:18:39.6	10.0	3.50	0.50	1.71	0.09
PPM 93747	4:46:10.3	27:29:25.4	10.2	2.91	0.43	1.73	0.10
HD 30190	4:46:33.0	27:54:02.5	8.4	3.76	0.44	1.40	0.09
HD 283851	4:46:42.9	27:15:42.2	10.7	3.89	1.07	1.71	0.17
PPM 93771	4:47:27.7	24:21:17.5	9.9	3.98	0.68	1.42	0.09
BD+27696	4:47:52.3	27:44:40.0	9.6	2.89	0.28	1.78	0.09
PPM 93776	4:47:54.1	26:33:38.4	10.3	2.85	0.54	1.25	0.10
PPM 93780	4:48:12.7	27:01:47.5	11.1	5.54	2.34	1.90	0.16
PPM 93819	4:50:58.5	24:16:42.8	11.0	4.38	1.57	1.66	0.14
BD+25740	4:51:10.9	25:37:20.9	10.8	3.86	0.69	2.82	0.16
PPM 93854	4:53:09.5	25:29:28.0	10.3	5.45	1.38	1.74	0.10

^{a} Apparent *V*-band magnitudes were obtained from the SIMBAD database, operated at CDS,
Strasbourg, France. References include Høg et al. (2000) and Adolfsson (1954).

3. RESULTS

3.1. *Polarization Fits*

Stokes parameters q and u, polarization amplitudes p, position angles θ, and uncertainties on each value, at each wavelength, are listed in Table 3 for the low-extinction sample and in Table 4 for the high-extinction star sample. The polarization amplitudes and angle uncertainties have been corrected for positive noise bias (e.g., Wardle & Kronberg 1974; Simmons & Stewart 1985; Vaillancourt 2006). For data with signal to noise in the range $p/\sigma_p > \sqrt{2}$ we use $p_{\rm corr} = (p^2 - \sigma_p^2)^{1/2}$ and $\sigma_\theta = 26.8° \times (\sigma_p/p_{\rm corr})$. For $p/\sigma_p \leq \sqrt{2}$ we set $p_{\rm corr} = 0$; in this case angle measurements are not meaningful so neither angles nor their uncertainties are listed.

As can be seen in Figure 3 (and gleaned from Tables 5 and 6), the polarization for most objects follows the expected form (equation 1), both for the case of fixing the parameter $K = 1.15$ (the "Serkowski" relation; Serkowski et al. 1975) and when K is a fitted quantity (the "Wilking" relation; Wilking et al.

Table 2. Stellar Target Sample for Optical Spectropolarimetry

Star[a]	Alternate Name	RA (J2000) (hh:mm:ss.s)	Dec. (J2000) (dd:mm:ss.s)	V[b] (mag.)	Spectral Class[c]	A_V[d] (mag.)	R_V[e] (mag.)	R_V[f] (mag.)	Source[g]	Distance[h] (pc)
SWIW 002		04:09:01.4	+24:53:21.4	12.9	K3	5.14±0.6	4.0±0.3	3.7±0.1	A	1030^{+158}_{-122}
SWIW 014		04:13:06.6	+22:35:36.5	13.4	M3	2.1±0.6	4.6±0.9	3.9±0.2	A	2658^{+568}_{-417}
SWIW 019		04:13:48.7	+28:23:43.6	14.0	K7	4.6±0.5	5.3±0.4	4.9±0.2	A	2128^{+394}_{-294}
SWIW 026		04:15:24.1	+28:07:07.4	14.7	F8	5.6±0.5	5.0±1.4	4.7±0.2	A	158^{+1}_{-1}
SWIW 040	V409 Tau	04:18:10.8	+25:19:57.4	12.5	M0e	5.5±0.6	$\cdots$	8.0±3.1	A	131^{+1}_{-1}
SWIW 046		04:19:58.3	+28:12:13.9	14.3	K4	4.5±0.5	5.3±0.1	4.9±0.1	A	1713^{+285}_{-217}
SWIW 049		04:20:41.4	+27:05:47.4	15.4	G9	6.7±0.6	5.1±0.1	4.8±0.1	S	614^{+31}_{-28}
SWIW 051		04:21:00.0	+30:22:17.9	13.8	M5	1.3±0.8	8.6±0.2	7.4±0.6	S(A)	2314^{+808}_{-520}
SWIW 057		04:23:17.8	+28:06:26.0	13.7	M4	2.8±0.8	4.1±0.6	3.6±0.2	A	3355^{+1015}_{-710}
SWIW 093		04:30:38.7	+22:55:52.0	17.1	K4	9.1±0.8	6.4±0.1	6.2±0.2	S	574^{+38}_{-34}
SWIW 100	JH 57	04:31:26.4	+27:07:20.4	14.7	F0	6.0±0.5	2.3±0.2	2.1±0.1	A	164^{+3}_{-3}
SWIW 101		04:31:31.6	+24:39:42.4	12.8	K3	4.2±0.6	4.0±0.4	3.6±0.1	A	966^{+98}_{-82}
SWIW 109		04:32:01.3	+28:13:34.7	13.5	K7	3.0±0.6	3±2	2.5±0.1	A	1973^{+409}_{-296}
SWIW 121	CoKu HK Tau G1	04:32:41.7	+24:19:03.8	16.1	F0	8.2±0.6	3.3±0.1	3.3±0.2	A	140^{+3}_{-3}
SWIW 125	JH 114	04:33:21.6	+22:39:50.4	13.4	K1	4.4±0.5	12.2±0.6	11.0±0.4	P	476^{+17}_{-16}
SWIW 144		04:34:38.5	+22:42:13.3	13.2	K1	4.8±0.6	5.3±0.1	4.9±0.1	P	380^{+11}_{-11}
SWIW 148	HO Tau	04:35:20.2	+22:32:14.6	14.5	M3e	$\cdots$	$\cdots$	$\cdots$		161^{+1}_{-1}
SWIW 158		04:36:30.0	+23:18:38.3	13.7	M2	3.6 ±0.9	2.7±0.1	2.4±0.1	A	2138^{+547}_{-378}
SWIW 159		04:36:35.1	+25:26:42.5	13.5	G7	4.9±0.9	5.7±0.1	5.1±0.1	A	823^{+74}_{-63}
SWIW 163		04:37:13.7	+24:22:20.8	13.5	K7	3.2±0.5	3.9±1.0	3.5±0.1	A	1710^{+330}_{-242}
SWIW 184	JH 214	04:39:07.0	+26:27:19.9	15.7	F0	6.2±0.6	2.8±0.1	2.7±0.1	S	287^{+9}_{-9}
HD 283809		04:41:24.9	+25:54:48.0	10.9	B3	5.3	3.5±0.2	3.3±0.1	A	323^{+10}_{-9}
SWIW217	Kim 1-69, JH 227	04:42:35.7	+25:27:15.2	12.8	K4	5.6±0.8	4.5±0.9	4.3±0.1	A	512^{+35}_{-31}
SWIW 230		04:43:48.7	+24:57:30.6	13.2	K7	3.8±0.5	4.6±0.8	4.2±0.1	A	979^{+159}_{-121}
Tamura 17	Kim 1-88	04:44:01.5	+25:20:13.0	11.1	M5	2.4±0.8	7.1±1.8	7.2±1.5	A	379^{+23}_{-20}

[a] SWIW refers to star numbers in the catalog of Shenoy et al. (2008).

[b] V-band brightnesses from the NOMAD[2] compilation.

[c] Spectral classes estimated from this work (see Section 2.3). Uncertainties on all classes are 1–2 subclasses.

[d] Extinction values from Shenoy et al. (2008).

[e] $R_V = 1.1 \cdot E(V-K)/E(B-V)$ based on the spectral classes given in column 6 and photometry from AAVSO (Henden et al. 2016), SDSS, and 2MASS

[f] R_V based on the spectral classes given in column 6 and fits of $E(\lambda-V)/E(B-V)$ using data from AAVSO (Henden et al. 2016), SDSS, 2MASS, and WISE

[g] Source of visual photometry in order of preference: A: AAVSO, S: SDSS, P: Panstarrs. For SWIW051, while AAVSO data exist, the resulting fits are poor.

[h] From Gaia DR2

1980). The change in the resulting goodness-of-fit (as measured using a standard reduced-χ^2; Tables 5 and 6) between these different options for K is marginal at best (the quoted χ^2 corresponds to a "Wilking fit" if a K-value is quoted, otherwise to a "Serkowski fit"). To check whether the additional term in the fit is statistically justified, we performed F-tests by calculating the quantity F_χ (e.g., Bevington & Robinson 1992). As reported in Tables 5 and 6, only 11 low-extinction stars and three high-extinction stars yield $F_\chi > 5$ (i.e., a >94% probability that the additional term is justified).

VAILLANCOURT ET AL.

Table 3. Photo-polarimetry Results from the Low-extinction Sample

Star	Wavelength[a] (μm)	q (%)	σ_q (%)	u (%)	σ_u (%)	p_{corr}[b] (%)	σ_p (%)	θ[c] (deg.)	σ_θ[b,c] (deg.)
PPM93195	0.36	−0.912	0.050	0.912	0.050	1.29	0.05	67.5	1.1
PPM93195	0.44	−1.104	0.039	1.044	0.039	1.52	0.04	68.3	0.8
PPM93195	0.55	−1.226	0.038	1.074	0.037	1.63	0.04	69.4	0.7
PPM93195	0.69	−1.111	0.029	1.081	0.029	1.55	0.03	67.9	0.6
PPM93195	0.83	−1.078	0.030	0.924	0.030	1.42	0.03	69.7	0.6
⋮	⋮	⋮	⋮	⋮	⋮	⋮	⋮	⋮	⋮
PPM93236	0.36	−0.007	0.017	0.019	0.020	0.00	0.02	⋯	⋯
PPM93236	0.44	−0.097	0.019	0.071	0.019	0.12	0.02	71.9	4.8
PPM93236	0.55	−0.150	0.020	0.002	0.025	0.15	0.02	89.6	3.9
PPM93236	0.69	−0.121	0.020	0.047	0.020	0.13	0.02	79.3	4.5
PPM93236	0.83	−0.074	0.031	0.067	0.032	0.10	0.03	69.0	9.0

[a] Wavelength centers for broad-band filters U, B, V, R, and I at NOT/Turpol are assigned as 0.36, 0.44, 0.55, 0.69, and 0.83 μm, respectively. Note these are not the same as the VRI-like bands defined for the Kast/Lick data (Appendix B; Table 9).

[b] Polarization amplitude and angle uncertainty are corrected for positive noise bias (Section 3.1).

[c] All angles are measured east of north. No values are reported for θ and σ_θ for cases in which the corrected polarization is set to zero.

NOTE—Polarization data for stars observed with the TurPol instrument on NOT. Listed uncertainties are statistical only and returned as part of the fitting procedure; uncertainties here do not include other systematics discussed in the text. (This table is available in its entirety in a machine-readable form in the online journal. A portion is shown here for guidance regarding its form and content.)

Table 4. Spectropolarimetry and H-band Results for the High-extinction Sample

Star	Wavelength[a] (μm)	q (%)	σ_q (%)	u (%)	σ_u (%)	p_{corr}[b] (%)	σ_p (%)	θ[c] (deg.)	σ_θ[c] (deg.)	χ_r^2[d]
SWIW 002	0.485	1.11	0.31	−3.77	0.31	3.92	0.31	143.2	2.2	0.79
SWIW 002	0.535	0.80	0.19	−4.29	0.19	4.36	0.19	140.3	1.2	0.44
⋮	⋮	⋮	⋮	⋮	⋮	⋮	⋮	⋮	⋮	⋮
SWIW 230	0.550	0.69	0.17	5.62	0.17	5.66	0.17	41.5	0.9	0.43
SWIW 230	0.650	0.57	0.19	5.40	0.19	5.42	0.19	42.0	1.0	0.36
SWIW 230	0.800	0.76	0.10	4.84	0.10	4.90	0.10	40.5	0.6	1.40
SWIW 230	1.630	0.91	0.14	1.39	0.14	1.65	0.14	28.4	2.4	⋯
⋮	⋮	⋮	⋮	⋮	⋮	⋮	⋮	⋮	⋮	⋮

[a] Data at wavelengths 0.550, 0.650 and 0.800 μm are binned centered at those wavelengths with full-widths of 0.100, 0.100, and 0.150 μm, respectively. Data at 1.630 μm are H-band data. All other wavelength points are binned with widths of 0.050 μm.

[b] Polarization amplitude and angle uncertainty are corrected for positive noise bias (Section 3.1).

[c] All angles are measured east of north. No values are reported for θ and σ_θ for cases in which the corrected polarization is set to zero.

[d] χ_r^2 values are not reported for H-band data.

NOTE—Polarization data for the high-extinction stars are listed here, with the exception of polarized standards (see Table 9). Listed uncertainties are statistical only and returned as part of the fitting procedure along with the reduced-χ^2 reported in the last column; uncertainties here do not include other systematics discussed in the text. (This table is available in its entirety in a machine-readable form in the online journal. A portion is shown here for guidance regarding its form and content.)

Table 5. Fitted Polarization Parameters and Measured Angles for the Low-extinction Sample

| | Serkowski ($K = 1.15$) and Wilking fits | | | | | | | | Position Angles | |
| | p_{max} | $\sigma_{P_{max}}$ | λ_{max} | $\sigma_{\lambda_{max}}$ | K | σ_K | χ_r^2 | F_χ [c] | $\langle\theta\rangle$ [a] | $\sigma_{\langle\theta\rangle}$ [a] |
Star	(%)	(%)	(μm)	(μm)					(deg.)	(deg.)
PPM 93181	0.87	0.02	0.59	0.02	$\cdots$	$\cdots$	0.54	0.2	98.8	1.5
PPM 93195	1.64	0.02	0.57	0.01	$\cdots$	$\cdots$	0.41	2.1	68.7	1.1
PPM 93213	0.72	0.04	0.48	0.04	$\cdots$	$\cdots$	0.4	0.4	127.7	4.6
PPM 93236	0.15	0.02	0.57	0.04	3.29	2.26	0.04	25.1	78.6	12.1
PPM 92238	1.2	0.01	0.57	0.01	$\cdots$	$\cdots$	0.33	1.3	104.1	1.5
PPM 93241	0.22	0.03	0.45	0.11	$\cdots$	$\cdots$	1.51	$\cdots$	51.8	11.4
PPM 93260	0.67	0.01	0.62	0.02	$\cdots$	$\cdots$	3.23	0.2	105.3	0.9
PPM 93265	0.95	0.03	0.72	0.03	$\cdots$	$\cdots$	1.01	0.1	23.4	2.5
PPM 93280	3.58	0.03	0.62	0.01	$\cdots$	$\cdots$	0.59	6.6	78.4	1
PPM 93281	0.59	0.05	0.54	0.02	2.89	0.94	0.92	3.7	69.9	3.9
PPM 93289	1.43	0.02	0.56	0.01	$\cdots$	$\cdots$	1.76	0	164.1	2.2
BD+27645	1.12	0.02	0.55	0.01	$\cdots$	$\cdots$	1.28	2.5	81	1.5
PPM 93320	0.66	0.03	0.59	0.04	$\cdots$	$\cdots$	0.81	1.6	63	2.3
BD+24636	0.77	0.04	0.63	0.05	$\cdots$	$\cdots$	0.44	0	19.4	2.8
PPM 93369	3.4	0.02	0.53	0.01	$\cdots$	$\cdots$	7.07	3.6	157.2	0.4
PPM 93376	2.83	0.02	0.68	0.01	$\cdots$	$\cdots$	2.02	0.1	108.7	1.5
PPM 93377	3.11	0.02	0.60	0.01	0.83	0.08	0.1	163.9	157.2	0.6
BD+25689	2.94	0.04	0.64	0.01	$\cdots$	$\cdots$	1.33	0.3	104.1	0.7
PPM 93390	2.4	0.03	0.60	0.01	$\cdots$	$\cdots$	0.87	2.8	57	0.7
PPM 93403	1.88	0.02	0.52	0.01	$\cdots$	$\cdots$	2.29	1.6	172.1	1.5
DB+25698	0.3	0.01	0.51	0.03	$\cdots$	$\cdots$	3.04	42.7	153	3.6
HD 283581	0.99	0.04	0.59	0.04	$\cdots$	$\cdots$	3.37	0.6	41.6	2.7
HD 283569	2.66	0.05	0.53	0.03	0.46	0.18	0.43	32.7	14	1
PPM 93449	0.61	0.02	0.55	0.03	$\cdots$	$\cdots$	0.65	0.5	10.2	2
PPM 93510	2.25	0.04	0.50	0.02	0.64	0.16	0.37	26.5	179.9	263.7
HD 283625	1.61	0.05	0.53	0.03	$\cdots$	$\cdots$	2.07	0.4	177.9	6
HD 28170	1.97	0.02	0.56	0.01	$\cdots$	$\cdots$	0.71	0.4	88	0.7
PPM 93537	2	0.01	0.55	0.01	$\cdots$	$\cdots$	2.23	5.3	12.4	0.6
PPM 93546	1.42	0.05	0.59	0.02	1.81	0.47	0.2	9.8	26	1.7
HD 28482	1.99	0.02	0.57	0.01	$\cdots$	$\cdots$	1.52	0.3	55.7	2.9
HD 28975	3.39	0.01	0.55	0.01	$\cdots$	$\cdots$	3.25	4.4	58.5	0.8
BD+26728	3.31	0.02	0.58	0.01	$\cdots$	$\cdots$	1.2	0	33.9	0.6
PPM 93637	1.69	0.01	0.54	0.01	$\cdots$	$\cdots$	2.48	1.7	33.1	0.3
PPM 93641	1.2	0.03	0.55	0.01	1.72	0.29	0.3	12.9	71.5	1.9
PPM 93642	1.71	0.02	0.57	0.01	$\cdots$	$\cdots$	0.23	1.1	69.4	2.2
PPM 93644	2.65	0.03	0.53	0.01	0.92	0.1	0.14	35.8	60.3	0.4
HD 29334	1.83	0.02	0.52	0.01	$\cdots$	$\cdots$	2.17	0.1	44.9	0.9
BD+27675	1.81	0.02	0.54	0.01	$\cdots$	$\cdots$	1.6	0.8	29.7	0.9
BD+22723	2.24	0.03	0.50	0.01	$\cdots$	$\cdots$	1.22	6.8	60.3	0.9
PPM 93658	2.41	0.02	0.53	0.01	$\cdots$	$\cdots$	1.11	2.9	56	0.6
PPM 93660	2.24	0.01	0.52	0.01	$\cdots$	$\cdots$	4.3	3	54.6	1
PPM 93668	1.03	0.01	0.65	0.01	$\cdots$	$\cdots$	4	0	41.5	0.9
PPM 93675	0.7	0.02	0.60	0.03	$\cdots$	$\cdots$	0.35	0.1	42.8	2.9
HD 283772	0.61	0.03	0.62	0.04	$\cdots$	$\cdots$	2.09	7	96.6	7.2
BD+25724	5.43	0.03	0.55	0.01	$\cdots$	$\cdots$	1.13	3.2	39.2	1.2
PPM 93713	2.88	0.02	0.55	0.01	0.95	0.07	1.42	5.1	43.8	0.3

Table 5 *continued*

VAILLANCOURT ET AL.

Table 5 *(continued)*

	Serkowski ($K = 1.15$) and Wilking fits								Position Angles	
	p_{max}	$\sigma_{P_{max}}$	λ_{max}	$\sigma_{\lambda_{max}}$	K	σ_K	χ_r^2	$F_\chi c$	$\langle\theta\rangle a$	$\sigma_{\langle\theta\rangle} a$
Star	(%)	(%)	(μm)	(μm)					(deg.)	(deg.)
BD+22741	2.32	0.03	0.51	0.01	$\cdots$	$\cdots$	0.57	0.3	61.4	0.8
PPM 93722	4.05	0.02	0.55	0.01	0.88	0.07	0.38	43.6	24.9	1
BD+25727	6.36	0.01	0.57	0.01	$\cdots$	$\cdots$	8.13	0.1	31.8	0.3
BD+26742	3.75	0.02	0.55	0.01	$\cdots$	$\cdots$	0.84	1.9	32.5	1.1
HD 30122	1.26	0.02	0.53	0.01	$\cdots$	$\cdots$	0.85	3	61.2	0.6
BD+26746	4.67	0.02	0.55	0.01	$\cdots$	$\cdots$	2.93	0.2	26.8	0.3
PPM 93747	3.48	0.02	0.54	0.01	$\cdots$	$\cdots$	3.44	0.7	40.8	0.6
HD 30190	3.7	0.02	0.55	0.01	$\cdots$	$\cdots$	1.18	0.4	56.4	0.3
HD 283851	3.15	0.03	0.57	0.01	$\cdots$	$\cdots$	0.31	0.3	40.9	0.6
PPM 93771	1.23	0.03	0.52	0.03	$\cdots$	$\cdots$	0.51	0.4	51	2.1
BD+27696	4.04	0.02	0.53	0.01	$\cdots$	$\cdots$	12.29	3.4	59.5	0.9
PPM 93776	3.62	0.02	0.55	0.01	$\cdots$	$\cdots$	1.39	0	33.3	0.7
PPM 93780	5.17	0.03	0.53	0.01	$\cdots$	$\cdots$	1.64	8.7	44.9	0.4
PPM 93819	1.29	0.04	0.46	0.02	$\cdots$	$\cdots$	3.1	0.6	49.4	1.6
BD+25740	3.52	0.03	0.55	0.01	$\cdots$	$\cdots$	1.84	0	40.7	0.5
PPM 93854	2.67	0.03	0.61	0.01	$\cdots$	$\cdots$	0.44	1.3	50.3	0.8
PPM 93181	0.85	0.02	0.57	0.02	$\cdots$	$\cdots$	0.57	0.3	98.8	1.5
PPM 93195	1.62	0.02	0.56	0.01	$\cdots$	$\cdots$	0.48	0.5	68.7	1.1
PPM 93213	0.72	0.04	0.47	0.04	$\cdots$	$\cdots$	0.57	0.4	127.7	4.6
PPM 93236	0.14	0.02	0.56	0.04	3.49	2.41	0.11	8.3	78.6	12.1
PPM 92238	1.18	0.01	0.56	0.01	$\cdots$	$\cdots$	0.09	0.2	104.1	1.5
PPM 93241	0.22	0.03	0.43	0.12	$\cdots$	$\cdots$	1.67	$\cdots$	51.8	11.4
PPM 93260	0.67	0.01	0.61	0.02	$\cdots$	$\cdots$	3.16	0.1	105.3	0.9
PPM 93265	0.95	0.03	0.72	0.04	$\cdots$	$\cdots$	0.73	0.3	23.4	2.5
PPM 93280	3.54	0.03	0.61	0.01	$\cdots$	$\cdots$	0.43	2.5	78.4	1.0
PPM 93281	0.59	0.04	0.52	0.02	3.23	1.03	0.78	5.2	69.9	3.9
PPM 93289	1.41	0.02	0.54	0.01	$\cdots$	$\cdots$	1.31	0.3	164.1	2.2
BD+27645	1.11	0.02	0.54	0.01	$\cdots$	$\cdots$	1.13	1.8	81.0	1.5
PPM 93320	0.65	0.03	0.58	0.04	$\cdots$	$\cdots$	0.86	3.2	63.0	2.3
BD+24636	0.77	0.04	0.63	0.05	$\cdots$	$\cdots$	0.42	0.0	19.4	2.8
PPM 93369	3.37	0.02	0.51	0.01	$\cdots$	$\cdots$	3.07	3.1	157.2	0.4
PPM 93376	2.82	0.02	0.67	0.01	$\cdots$	$\cdots$	4.19	0.4	108.7	1.5
PPM 93377	3.09	0.02	0.59	0.01	0.87	0.08	0.18	62.9	157.2	0.6
BD+25689	2.92	0.04	0.64	0.02	$\cdots$	$\cdots$	1.03	0.5	104.1	0.7
PPM 93390	2.37	0.03	0.59	0.01	$\cdots$	$\cdots$	0.71	1.8	57.0	0.7
PPM 93403	1.86	0.02	0.51	0.01	$\cdots$	$\cdots$	1.47	1.5	172.1	1.5
BD+25698	0.30	0.01	0.50	0.03	$\cdots$	$\cdots$	2.73	32.9	153.0	3.6
HD 283581	0.98	0.04	0.59	0.04	$\cdots$	$\cdots$	3.54	0.4	41.6	2.7
HD 283569	2.65	0.04	0.52	0.02	0.49	0.20	0.42	26.8	14.0	1.0
PPM 93449	0.61	0.02	0.54	0.03	$\cdots$	$\cdots$	0.84	0.4	10.2	2.0
PPM 93510	2.24	0.03	0.49	0.02	0.67	0.17	0.46	17.6	179.9	0.3
HD 283625	1.60	0.05	0.52	0.03	$\cdots$	$\cdots$	2.41	0.4	177.9	6.0
HD 28170	1.94	0.02	0.55	0.01	$\cdots$	$\cdots$	1.06	1.0	88.0	0.7
PPM 93537	1.98	0.01	0.53	0.01	$\cdots$	$\cdots$	1.69	2.4	12.4	0.6
PPM 93546	1.40	0.05	0.58	0.02	1.92	0.50	0.13	17.9	26.0	1.7
HD 28482	1.97	0.02	0.56	0.01	$\cdots$	$\cdots$	1.78	0.0	55.7	2.9
HD 28975	3.35	0.01	0.54	0.01	$\cdots$	$\cdots$	1.46	3.3	58.5	0.8
BD+26728	3.27	0.02	0.57	0.01	$\cdots$	$\cdots$	1.49	0.1	33.9	0.6
PPM 93637	1.67	0.01	0.53	0.01	$\cdots$	$\cdots$	0.60	1.2	33.1	0.3
PPM 93641	1.19	0.03	0.54	0.01	1.81	0.31	0.84	5.4	71.5	1.9

Table 5 *continued*

Table 5 *(continued)*

	Serkowski ($K = 1.15$) and Wilking fits								Position Angles	
	p_{max}	$\sigma_{P_{max}}$	λ_{max}	$\sigma_{\lambda_{max}}$	K	σ_K	χ^2_r	F_χ^c	$\langle\theta\rangle^a$	$\sigma_{\langle\theta\rangle}^a$
Star	(%)	(%)	(μm)	(μm)					(deg.)	(deg.)
PPM 93642	1.69	0.02	0.55	0.01	$\cdots$	$\cdots$	0.39	0.0	69.4	2.2
PPM 93644	2.63	0.02	0.52	0.01	0.98	0.11	0.15	15.4	60.3	0.4
HD 29334	1.81	0.02	0.50	0.01	$\cdots$	$\cdots$	0.54	0.1	44.9	0.9
BD+27675	1.79	0.02	0.53	0.01	$\cdots$	$\cdots$	1.27	0.4	29.7	0.9
BD+22723	2.22	0.03	0.49	0.01	$\cdots$	$\cdots$	0.79	2.3	60.3	0.9
PPM 93658	2.38	0.02	0.51	0.01	$\cdots$	$\cdots$	0.09	2.6	56.0	0.6
PPM 93660	2.23	0.01	0.51	0.01	$\cdots$	$\cdots$	2.35	0.5	54.6	1.0
PPM 93668	1.02	0.01	0.64	0.02	$\cdots$	$\cdots$	4.46	0.1	41.5	0.9
PPM 93675	0.69	0.02	0.59	0.03	$\cdots$	$\cdots$	0.35	0.4	42.8	2.9
HD 283772	0.61	0.03	0.61	0.04	$\cdots$	$\cdots$	1.98	7.3	96.6	7.2
BD+25724	5.36	0.03	0.53	0.01	$\cdots$	$\cdots$	1.20	0.6	39.2	1.2
PPM 93713	2.86	0.02	0.54	0.01	0.98	0.08	0.28	17.5	43.8	0.3
BD+22741	2.30	0.03	0.50	0.01	$\cdots$	$\cdots$	0.87	0.0	61.4	0.8
PPM 93722	4.04	0.02	0.53	0.01	0.96	0.07	0.36	19.1	24.9	1.0
BD+25727	6.28	0.01	0.56	0.01	$\cdots$	$\cdots$	3.56	0.0	31.8	0.3
BD+26742	3.70	0.02	0.54	0.01	$\cdots$	$\cdots$	0.48	0.7	32.5	1.1
HD 30122	1.27	0.02	0.51	0.01	1.59	0.24	0.23	14.8	61.2	0.6
BD+26746	4.61	0.02	0.53	0.01	$\cdots$	$\cdots$	2.48	2.1	26.8	0.3
PPM 93747	3.44	0.02	0.53	0.01	$\cdots$	$\cdots$	1.39	0.3	40.8	0.6
HD 30190	3.66	0.02	0.54	0.01	$\cdots$	$\cdots$	0.14	0.0	56.4	0.3
HD 283851	3.11	0.03	0.56	0.01	$\cdots$	$\cdots$	0.30	0.1	40.9	0.6
PPM 93771	1.22	0.03	0.51	0.03	$\cdots$	$\cdots$	0.71	0.4	51.0	2.1
BD+27696	4.00	0.02	0.51	0.01	$\cdots$	$\cdots$	5.64	2.0	59.5	0.9
PPM 93776	3.58	0.02	0.54	0.01	$\cdots$	$\cdots$	1.60	0.2	33.3	0.7
PPM 93780	5.11	0.03	0.52	0.01	$\cdots$	$\cdots$	0.57	1.7	44.9	0.4
PPM 93819	1.29	0.04	0.44	0.02	$\cdots$	$\cdots$	2.57	1.8	49.4	1.6
BD+25740	3.47	0.03	0.54	0.01	$\cdots$	$\cdots$	1.95	0.0	40.7	0.5
PPM 93854	2.64	0.03	0.60	0.01	$\cdots$	$\cdots$	0.35	0.5	50.3	0.8

NOTE—Parameters p, λ_{max}, K (Wilking), and their uncertainties are fitted to all stars, as are parameters where $K = 1.15$ (Serkowski). Here we report the three Wilking fit parameters only if an F-test of the extra term in the Wilking relation returns $F_\chi > 5$, otherwise the Serkowski values are reported. These fits are discussed in Appendix C.

^a $F_\chi \equiv (\chi^2_s - \chi^2_w)/(\chi^2_w/N)$, where N is the number of degrees of freedom in the fits and $\chi_{s,w}$ are the χ^2_r reported in the table for the fits to the Serkowski and Wilking relations, respectively.

^b $\langle\theta\rangle$ is the variance-weighted mean (calculated in Stokes-space) of the measured position angles in the five broadbands *UBVRI* in this work. $\sigma_{\langle\theta\rangle}$ is the larger of the median uncertainty or unweighted standard deviation of the five angles.

Table 6. Fitted Polarization Parameters and Measured Angles for High-extinction Stars

	Serkowski ($K = 1.15$) and Wilking fits								Position Angles			
	p_{max}	$\sigma_{P_{max}}$	λ_{max}	$\sigma_{\lambda_{max}}$	K	σ_K	χ^2_r	F_χ^a	$\langle\theta\rangle^b$	$\sigma_{\langle\theta\rangle}^b$	$\theta(\mathrm{IR})^c$	$\sigma_{\theta(\mathrm{IR})}$
Star	(%)	(%)	(μm)	(μm)					(deg.)	(deg.)	(deg.)	(deg.)
					Fits include H-band data							
SWIW 002	5.29	0.08	0.762	0.015	1.53	0.22	0.05	61.7	142.4	1.1	133.6	5.4
SWIW 014	1.48	0.07	0.679	0.065	$\cdots$	$\cdots$	0.34	0.3	111.5	4.4	89.7	21.2

Table 6 *continued*

Table 6 *(continued)*

	Serkowski ($K = 1.15$) and Wilking fits								Position Angles			
	p_{max}	$\sigma_{P_{max}}$	λ_{max}	$\sigma_{\lambda_{max}}$	K	σ_K	χ_r^2	F_χ[a]	$\langle\theta\rangle$[b]	$\sigma_{\langle\theta\rangle}$[b]	θ(IR)[c]	$\sigma_{\theta(IR)}$
Star	(%)	(%)	(μm)	(μm)					(deg.)	(deg.)	(deg.)	(deg.)
SWIW 019	2.81	0.07	0.655	0.031	⋯	⋯	0.20	1.8	172.3	2.2	152.5	4.8
SWIW 026	3.60	0.09	0.896	0.035	⋯	⋯	0.49	0.1	21.1	4.9	8.5	2.9
SWIW 046	4.68	0.07	0.610	0.015	⋯	⋯	0.26	1.9	7.0	1.1	4.5	2.3
SWIW 049	2.56	0.08	0.652	0.034	⋯	⋯	0.95	2.6	40.8	2.3[d]	32.1	4.3
SWIW 057	6.60	0.13	0.587	0.014	⋯	⋯	2.05	0.6	1.7	1.3	171.3	2.1
SWIW 093	1.44	0.14	0.808	0.141	⋯	⋯	0.50	0.2	74.2	12.1	49.2	9.9
SWIW 100	1.78	0.14	1.131	0.092	⋯	⋯	0.70	1.3	20.2	5.3	12.0	4.9
SWIW 101	3.82	0.05	0.712	0.020	⋯	⋯	0.26	3.0	76.7	1.5	72.1	4.5
SWIW 109	2.85	0.09	0.567	0.035	⋯	⋯	0.06	1.1	40.4	3.2	17.5	7.0
SWIW 121[e]	3.08	0.71	0.384	0.074	⋯	⋯	0.31	0.1	85.3	19.9	139.2	14.4
SWIW 125	2.41	0.07	0.585	0.068	0.81	0.30	0.20	6.6	53.8	2.1	40.8	6.1
SWIW 144	2.03	0.06	0.751	0.047	⋯	⋯	0.37	1.5	26.5	5.7	4.2	11.5
SWIW 148	1.26	0.06	0.628	0.061	⋯	⋯	0.20	0.0	55.9	4.5	7.4	18.4
SWIW 158	5.14	0.09	0.593	0.017	⋯	⋯	0.12	0.0	51.5	1.6	35.8	6.9
SWIW 159[e]	4.19	0.31	0.412	0.093	0.52	0.16	0.33	46.0	44.0	2.3	27.1	2.7
SWIW 163	4.24	0.08	0.588	0.019	⋯	⋯	0.58	2.9	52.5	1.5	52.5	4.9
SWIW 184	2.11	0.12	0.628	0.060	⋯	⋯	0.30	0.1	55.7	4.1	48.1	8.1
SWIW 230	5.60	0.10	0.567	0.014	⋯	⋯	0.24	1.7	41.2	1.4	28.4	2.4
No *H*-band data												
SWIW 040[e]	6.50	0.28	1.242	0.049	⋯	⋯	0.38	0.4	50.1	2.4	49.7	0.4
HD 283809	6.68	0.14	0.610	0.022	⋯	⋯	0.01	0.1	53.6	2.5	54.5	0.4
Kim 69	7.80	0.09	0.623	0.014	⋯	⋯	0.03	0.4	44.9	1.6	44.5	⋯
Tamura 17	5.78	0.13	0.555	0.017	⋯	⋯	0.03	0.7	45.4	1.6	44.6	⋯

NOTE—Parameters p, λ_{max}, K (Wilking), and their uncertainties are fitted to all stars, as are parameters where $K = 1.15$ (Serkowski). Here we report the three Wilking fit parameters only if an F-test of the extra term in the Wilking relation returns $F_\chi > 5$, otherwise the Serkowski values are reported. These fits are discussed in Appendix C.

[a] $F_\chi \equiv (\chi_s^2 - \chi_w^2)/(\chi_w^2/N)$, where N is the number of degrees of freedom in the fits and $\chi_{s,w}$ are the χ_r^2 reported in the table for the fits to the Serkowski and Wilking relations, respectively.

[b] $\langle\theta\rangle$ is the variance-weighted mean (calculated in Stokes-space) of the measured position angles in the 11 optical wavelengths in this work. $\sigma_{\langle\theta\rangle}$ is the larger of the median uncertainty or unweighted standard deviation of the 11 angles.

[c] θ(IR) is the position angle measured in *H*-band for all SWIW-objects. For HD 283809 this value is the mean angle at $\lambda = 0.35$–2.2 μm from Whittet et al. (2001). For Kim 69 and Tamura 17 the angles are from the *K*-band measurements of Tamura et al. (1987).

[d] Calculation of $\sigma_{\langle\theta\rangle}$ does not include outliers at 0.485 and 0.985 μm.

[e] The collected data for SWIW 040, 121, 159, and PPM 93780 do not bracket a wavelength peak. Therefore, the p_{max} and λ_{max} values here are likely unreliable.

Of the stars studied here, spectropolarimetry has previously been performed for only HD 283809, for which Whittet et al. (2001) found $p_{max} = 6.70 \pm 0.10\%$, $\lambda_{max} = 0.59 \pm 0.02\,\mu$m, and $K = 0.97 \pm 0.10$. Within the uncertainties, these values are consistent with the values found here.

The stars SWIW 121 and SWIW 159 show no clear peak of polarization with wavelength longward of the shortest measured wavelength of $0.460\,\mu$m. As a result, fits to find a peak (p_{max}, λ_{max}) are unreliable. In SWIW 121, this was most likely due to very low signal-to-noise in the polarization signal and is also reflected in the large λ_{max} uncertainty when K was allowed to float. The signal-to-noise was adequate for SWIW 159, so it is likely that λ_{max} is intrinsically small. A weighted Serkowski fit to the optical data yields ($p_{max} = 3.87\% \pm 0.08\%$, $\lambda_{max} = 0.59 \pm 0.02\,\mu$m, $\chi^2 = 3.1$). Data and fit values for these two stars are not included in Figure 5.

The Lick/Kast polarization data for SWIW 040 continues to increase up to the longest measured wavelength of $1.01\,\mu$m and neither the Serkowski nor the Wilking fits yield a peak at shorter wavelengths. A weighted Serkowski fit to the optical data yields ($p_{max} = 6.45\% \pm 0.30\%$, $\lambda_{max} = 1.24 \pm 0.05\,\mu$m, $\chi^2 = 3.6$). Due to the high S/N of this fit and the data, we include this star in the analysis, and note that its inclusion alters the fit parameters of the "upper branch" by less than 2σ (Section 4.1 and equation [3]).

For SWIW 051, all data, with the exception of the $0.685\,\mu$m bin and *H*-band, are consistent with zero polarization. Therefore, no fits are reported for that star in Table 6.
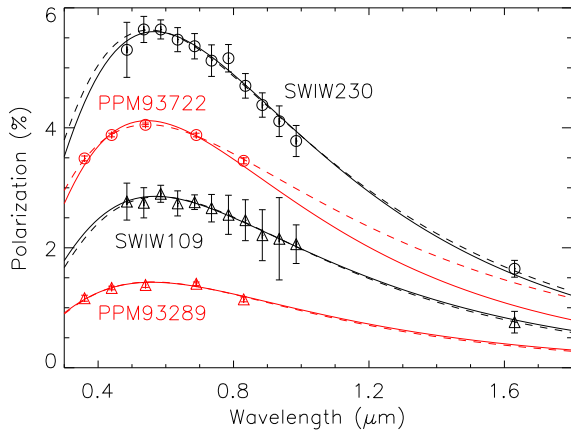
Figure 3. Example fits to the Serkowski curve for four stars. Black circles and triangles represent data for two high-extinction stars at 11 optical wavelengths bins and *H*-band, while the red points represent low-extinction stars at the *UBVRI* passbands only. Solid lines represent fits to the Serkowski relation (with parameter *K* = 1.15) whereas *K* is allowed to float in the dashed-line fits to the Wilking relation.

Figure 4. Stacked histograms of position angle differences with a $0°\!.5$ binsize. For each star, position angle differences were determined with respect to the median position angle measured for that star across the optical wavelength bins. The numbers in each Kast and TURPOL data were normalized by the total number of wavelength bins so that the total area under the Kast and TURPOL histograms represents the total number of stars in the sample and is not biased by the different number of wavelength samples. The standard deviation of the low- and high-extinction distributions ($3°\!.7$ and $4°\!.1$, respectively) are only slightly larger than typical angle uncertainties (e.g., Appendix B.3).

The spectra of the stars observed with Lick/Kast exhibit several strong telluric absorption lines. The molecular oxygen A-band (0.760–0.763 μm) is by far the strongest of these and may lead to contamination of the 0.785 μm bin. This was particularly evident for SWIW 049 and for SWIW 144, where the polarization curve showed an unexpected "dip" compared to its nearest spectral bins. However, removal of the A-band lines from the 0.785 μm bin did not change this behavior and the change in the resulting polarization (both amplitude and angle) was within the uncertainties given in Table 4. Therefore, we do not expect any telluric absorption lines have a significant effect on the polarization data reported here.

3.2. *Polarization Angles*

The optical position angles in most of our sample are consistent with constant angles across all measured wavelength bins. Position angle differences with respect to the median angle for each star are shown in Figure 4. For each star, position angle differences were determined with respect to the median position angle measured for that star across the optical wavelength bins. (Thus, the *H*-band angle difference is not included in the median, but is plotted here as the difference with respect to the median angle in the optical data.) Due to the odd number of wavelength samples (11 and 5 for the Kast and TURPOL data, respectively), one angle-difference sample is always precisely zero when the median is subtracted; those data are not plotted in Figure 4. The numbers in each Kast and TURPOL data bin were normalized by the total number of wavelength samples so that the total area under the Kast and TURPOL histograms represents the total number of stars in the sample and is not biased by the different number of wavelength samples.

The standard deviations of the angle differences for the low- and high-extinction distributions are $3°\!.7$ and $4°\!.1$, respectively. These standard deviations are similar to typical uncertainties on the angle measurements for each star in each wavelength

bin, $\sim 2°$–$5°$. In the low-extinction sample, only HD 283772 shows a significant rotation of position angles, from about $107°$ to $92°$ across *U*- to *I*-band, with uncertainties of $2°$–$3°$ per band. Two stars in the high-extinction sample show significant rotation over the wavelength span. The angles for SWIW 026 rotate from about $20°$–$25°$ at $0.5\,\mu$m to $8°$ at $1\,\mu$m, with typical uncertainties of $1°$–$3°$ per bin. The angles for SWIW 144 rotate from about $35°$ at $0.5\,\mu$m to about $20°$ at $1\,\mu$m, with typical uncertainties of $2°$–$4°$ per bin.

The last four columns of Table 6 compare the optical and infrared position angles for the 24 high extinction stars with fits. The mean optical position angles $\langle\theta\rangle$ are calculated by averaging the (variance-weighted) Stokes parameters for all 11 bins. As an estimate of the uncertainty, we use the larger of the standard deviation of the 11 angle measurements or the median angle uncertainty of the 11 bins. We make this conservative choice in order to consider both statistical and systematic uncertainties in the angle measurements. Angles and uncertainties for the 20 stars with *H*-band data are given the in the θ(IR) and σ_θ(IR) columns. For the four stars without *H*-band data, we use other measurements from the literature (see references in Table) to estimate θ(IR) and σ_θ(IR).

The optical angles for these last four stars are in excellent agreement with the existing IR measurements, within the uncertainties of $1°$–$2°$. However, the difference between the other *H*-band and optical angles are larger (see the red bins in Fig. 4). Most significantly the optical and IR angles for stars SWIW 019, 057, 159, and 230 differ by more than three times their uncertainties.

3.3. *Notes on Individual Stars*

The goal of our work is to measure the polarization that the molecular cloud imposes on unpolarized starlight. Systematic biases will arise in this measurement if any stars exhibit intrinsic polarization, such as may occur with disks and other matter around young stars. We check for this possibility using observational tracers of circumstellar matter, such as infrared (IR) excesses, or for indications that the star is young, such as emission lines.

A physical association with the molecular cloud may be an indication of young age and possible presence of circumstellar material. We first check for such an association by comparing the distances of the cloud to the distances of the stars in our sample. Distances to the stars listed in Table 2 are obtained from the Gaia Data Release 2 parallax survey (Gaia Collaboration et al. 2018; Bailer-Jones et al. 2018). Galli et al. (2019) used Gaia DR2 and radio VLBI astrometry to map the Taurus molecular cloud complex in three dimensions; they find that B215 is the closest sub-structure in the complex at a distance of $d = 128.5 \pm 1.6$ pc, while L1558 is the most remote at $d = 198.1 \pm 2.5$ pc.

Of our low extinction sample (Table 1), the star BD+25 698 ($d = 121 \pm 1$ pc) is located closer than B215 and an additional 11 sources are at distance between the cloud extremes of 130 and 200 pc (PPM- 93675, 93537, 93510, 93537, 93641, 93181, 93637, 93280; HD- 29334, 28170, 28975). None of these stars are found in catalogs of young stellar objects in Taurus (Herbig & Bell 1988a; Rebull et al. 2010, 2011; Herczeg & Hillenbrand 2014). Hence the low-extinction sample is unlikely to contain any sources with significant circumstellar polarization.

Of the high-extinction sample (Table 2), five stars lie within the range 130 to 200 pc (SWIW- 026, 040, 100, 121, 148). Two of these stars are fairly distant from dense regions of the cloud and thus unlikely to be YSOs associated with the cloud:

- SWIW026 ($d = 158 \pm 1$ pc) is projected closest to L1459 and "Cluster 7" of Galli et al. (2019) at a distance of 130 ± 1 pc.

- SWIW100 ($d = 164 \pm 3$ pc) is located between L1495, probed by cluster 7 at 130 ± 1 pc, and Heiles Cloud 2, probed by clusters 14 and 15 at 142 ± 2 pc and 138 ± 2 pc, respectively.

While SWIW 121 is close to L1531, it is most likely a Main Sequence star, not a YSO. Based on our Lick/Kast spectra, we classify the star as F0, with no observable emission lines. Similarly, no emission lines were observed by Cohen & Kuhi (1979) who classify the star as B2.

The remaining two stars are quite close to dense regions of the cloud, increasing the likelihood that they are YSOs associated with the cloud.

- SWIW040 ($d = 131 \pm 1$ pc) is projected closest to L1506, which is in line on the sky with B215 which is probed by "cluster 2", estimated to have a distance of 129 ± 2 pc.

- SWIW148 (161 ± 1 pc) is close to L1536 probed by cluster 16 at 160 ± 3 pc.

Additionally, SWIW 040 and SWIW 148 are T-Tauri stars (Romano 1975; Kenyon et al. 1994; Herbig & Bell 1988b) that exhibit emission lines in our Lick/Kast spectra. Emission lines in SWIW 040 were also observed by (Luhman et al. 2009) and Herczeg & Hillenbrand (2014), and Akimoto & Itoh (2019) attributes sporadic dimming of SWIW 040 to obscuration by a distorted circumstellar disk. Emission lines in SWIW 148 were also observed by Herczeg & Hillenbrand (2014).

To further investigate the status of these stars, we used the "Virtual Observatory Spectral Energy Density Analyzer" (VOSA) on-line tool (Bayo et al. 2008) to perform spectral energy distribution (SED) fitting for the SWIW stars. This Virtual Observatory tool uses archival photometry spanning the UV (GALEX) to mid-infrared (WISE), and allows fits based on many templates. We used blackbody curves as well as stellar models from the Coelho (2014) compilation. The derived spectral classes and extinctions are in good agreement with our spectral classifications (Table 2) and the extinction values from Shenoy et al. (2008). In this SED fitting, SWIW 040 and SWIW 148 show clear evidence for infrared excess. SWIW 121 displays a marginal and wavelength-independent IR excess possibly indicative of a debris disk. (Note that an IR excess does not necessarily imply intrinsic polarization, as a circumstellar disk that does not intercept the line of sight will cause IR excess, but not polarization.)

4. DISCUSSION

4.1. *Extinction vs. $\lambda_{\max}$*

As discussed in the introduction, radiative grain alignment theory predicts a dependence of the alignment efficiency on the color of the radiation field and the grain sizes, such that a grain of radius a is efficiently aligned when exposed to light of wavelength $\lambda < 2a$ (unless the grain collision rate is large— see below). Therefore, as the color of the aligning radiation field becomes redder (e.g., due to extinction) the size of the smallest *aligned* grain ($b_{\min} \approx \lambda/2$) shifts to larger sizes, even as the small-grain end of the total (aligned + unaligned) dust distribution remains fixed at $a_{\min} < b_{\min}$. Thus one expects $\lambda_{\max}$ to increase with increasing A_V.

In order to assess the trends and differences in the data presented here, we fit linear relations to various data subsets according to

$$\lambda_{\max} = \alpha + \beta A_V \qquad (3)$$

(see also equation [2]). The parameters, and parameter uncertainties, of this linear model are given in Table 7. Three sets of low-extinction data (presented as separate rows in the table) include the sample of Whittet et al. (2001), the TurPol sample from this work (Table 1), and the combined Whittet et al. and TurPol samples. These data yield similar results, with $\lambda_{\max}(\mu m) \sim 0.52 + 0.02 A_V$. A fit to the complete data set varies only slightly from the low-extinction data—the linear terms are the same (0.02 μm/mag) and the constant term is 0.51 μm.

While both terms for the "all data" case are similar to those of the low-extinction samples, the uncertainty in the offset is larger in the "all data" case. The cause of this much larger

Table 7. λ_{max}-A_V Relations

Data Set	Number of Stars	α (μm)	σ_α (μm)	β (μm/mag)	σ_β (μm/mag)	A_V (mag)
Whittet et al. (2001)[a]	20	0.53	0.01	0.020	0.004	0–4
TURPOL, this work	62	0.524	0.003	0.017	0.001	0–3
TURPOL + Whittet et al. (2001)	82	0.516	0.002	0.021	0.001	0–4
all data in this work	103	0.508	0.016	0.0219	0.0007	0–10
Lower Branch	96	0.513	0.002	0.019	0.001	0–6
Upper Branch	7	−0.015	0.10	0.17	0.02	0–10
Upper Branch, wo/SWIW040	6	0.17	0.11	0.12	0.02	0–10

NOTE—Various subsets of data are fit to the linear relation $\lambda_{max} = \alpha + \beta A_V$. All fits are weighted by data uncertainties. Data presented in this work are given in Tables 1, 2, 5, and 6 and plotted in Figure 5.

[a] Re-analyzed by Andersson & Potter (2007).

dispersion is a number of outliers that systematically deviate from the low-extinction fits around $A_V = 3$–6 mag (Figures 5a–b).

We split these points (SWIW 002, 019, 026, 040, 100, 101 and 144) into an "upper" branch and leave the remaining points in a "lower" branch. Separate linear fits to each branch are given in Table 7. It is unlikely that the "upper branch" is only the result of noisy data as an F-test finds that the addition of the "upper branch" is justified at more than the 99% probability level. Additionally, the fit to the "upper branch" is fairly robust against outliers—if SWIW 040, the star with the largest value of λ_{max} which is likely affected by instrinsic polarization from a circumstellar disk of dust (Akimoto & Itoh 2019; Section 3.3), is excluded—the parameters of the upper branch best fit are within 2σ of the fits to the complete upper branch (Table 7). We also note that the seven upper-branch stars are scattered throughout the cloud, not clustered in any single region (Figure 1), eliminating the possibility that the upper-branch is a localized effect.

4.2. *Position Angles*

A detailed study of the angle differences, and their causes, is beyond the scope of this work, but we note that the stars SWIW 019, 026 and 144 show significant angle rotations with wavelength, well beyond the measurement uncertainties. These stars all lie on the "upper branch" in the λ_{max}-A_V relation. A similar effect has been demonstrated for the star Elias 3-16 over the NIR range by Hough et al. (1988, 2008). For that star, those authors find that the position angle of the continuum polarization outside the the 3.1 μm H_2O ice and the 4.7 μm CO ice lines are $73° \pm 1.5°$ and $73° \pm 2.3°$, respectively. Inside the two ice lines the position angles rotate to $76° \pm 1.4°$ in the H_2O ice line and $86° \pm 4.2°$ in the CO-ice feature. The ice lines probe only material at large extinction ($A_V > 3.2$ mag for H_2O ice and $A_V > 6.7$ mag for CO ice (Whittet et al. 2007)), so the polarization inside the lines probes magnetic fields at larger optical depths than the continuum, where the weighting is more uniform along the line of sight.

We argue that the observed position angle rotation on the "upper branch" can be understood in a similar way. These lines

of sight likely probe both denser clumps as well as inter-clump gas. The grain growth in the dense clumps however means that for the longest wavelengths a relatively larger part of the polarization originates in the clumps. A systematic rotation in the magnetic field direction, between the clump and inter-clump gas should therefore show up as a rotation in the position angle with wavelength. If this scenario is correct, densely sampled multi-band (and ice line) polarimetry could be used to probe the line-of-sight geometry of the ordered magnetic field.

4.3. *A Grain Alignment Model*

The key point in our analysis is that the shape of polarization spectrum (Eq. 1) is related to the dust-grain size distribution. Any parameter that increases/decreases the size of the smallest aligned grain, b_{min}, shifts the peak in the polarization spectrum to longer/shorter wavelengths. (A similar relation holds between the spectrum and changes to the size of the largest aligned grain, b_{max}). This spectral shift is parameterized by λ_{max} in Eq. 1.

The physical parameters of the aligned-grain size distribution are a function of the underlying, total grain-size distribution and a balance between processes that tend to align the grains and processes that tend to dis-align the grains (Draine & Lazarian 1998). Here, we consider how the values of b_{min} and b_{max} vary in different interstellar environments by applying RATs to align the grains and gas-grain collisions to dis-align the grains. The inputs to our model include

- A power-law form for the underlying grain-size distribution as given by Mathis et al. (1977, MRN), but without the exponential extension proposed by later analyses (e.g., Kim & Martin 1995; Clayton et al. 2003).

- Gas-grain collision rates follow from the gas volume density n and temperature T. Assuming that a grain will become disaligned once it has collided with its own mass in gas particles, the disalignment rate is proportional to (Hoang et al. 2015)

$$R_{dis} \propto \frac{n \times \sqrt{T_{gas}}}{a}. \tag{4}$$

Thus, smaller grains are more efficiently disaligned by gas-grain collisions. For all models presented here we set the temperature to a constant value of 20 K. This simplification should not significantly affect our results as the collision rate is only a weak function of temperature ($R \sim T^{1/2}$).

- Radiative torques are calculated using the local interstellar radiation field, as estimated by Mathis et al. (1983), and its extinction as a function of depth into the cloud. Radiative transfer is performed in only one dimension, using a plane-parallel slab geometry with the aforementioned single space density per model.

While the RATs are dependent upon the radiation field (including its extinction A_V) and hence the *column density*, the collisional disalignment is dependent upon the gas *volume density*. Without independent data on the volume density, we would have to assume a physical path length in order to derive an average volume density from the measured extinctions. Instead, we selected gas density values in the range $n_{gas} \sim 10^2$–$10^4 \, \text{cm}^{-3}$. We also note that detailed three-dimensional modeling of radiative transfer and grain alignment, which incorporates realistic cloud structures (e.g., self consistent density and temperature profiles or an explicit clumpy structure with both clump and inter-clump gas in the same line of sight), is beyond the scope of this work.

Model results are shown in Figure 5c and compared to the data in Figure 5d. The primary features of the model plots are (1) at low extinction, $\lambda_{\max}$ has a minimum that varies with volume density but is independent of $b_{\max}$; (2) for models with the same volume density $\lambda_{\max}$ reaches a maximum that increases as $b_{\max}$ increases. For example, models 2 and 3, both with a density of $10^4 \, \text{cm}^{-3}$, converge at $\lambda_{\max} = 0.55 \, \mu\text{m}$. The divergence of these two models above an extinction of 6 mag is due to the different values of $b_{\max}$. Similarly, models 4, 5, and 6, all with a density of $4 \times 10^4 \, \text{cm}^{-3}$, converge at $\lambda_{\max} = 0.65 \, \mu\text{m}$ but diverge at moderate extinction levels, reaching larger values of $\lambda_{\max}$ as $b_{\max}$ increases from 0.3 to 0.7 μm.

4.4. *Dispersion in $\lambda_{\max}(A_V)$*

At low extinctions ($<4 \, \text{mag}$; particularly near $A_V = 1.5$–2.5 mag) the expanded sample shows an enhanced dispersion of $\lambda_{\max}$ compared to the Whittet et al. (2001) sample. Thus, the size distributions of aligned grains must differ along these lines of sight, despite having similar extinction levels (also see Wang et al. 2017).

For a given extinction level, one expects the radiation fields to be similar, unless the extinction from the observer through the target cloud region is not well-correlated with the extinction to the cloud grains from the illuminating source. However, stars with obvious anomalous sightlines were pre-screened (e.g., Andersson & Potter 2007) and removed from the list of targets in Table 1.

Another possibility for this dispersion is grain growth. The ratio of total-to-selective extinction, R_V, is generally correlated with grain size (Nozawa 2016; Cardelli et al. 1988). Estimates of R_V for the low-extinction line-of-sight sample (Table 1) are found using spectral classifications (Wright et al. 2003) and optical and NIR photometry (Høg et al. 2000; Skrutskie et al. 2006). For the extinction ranges $A_V = 0.5$–1.5, 1.5–2.5 and 2.5–3.5 mag, R_V has average values of 3.20 ± 0.08, 3.27 ± 0.07 and 3.66 ± 0.27, respectively (data in Table 1). Restricting the middle range of A_V to only stars with a large deviation ($\delta\lambda_{\max} > +0.05 \, \mu\text{m}$) from the linear $\lambda_{\max}$-A_V relation, the average is unchanged at $\langle R_V \rangle = 3.21 \pm 0.19$. These small variations in R_V yield no strong evidence for grain growth within or between these three extinction ranges.

Thus the increased dispersion of $\lambda_{\max}$ for the low extinction sightlines is unlikely to be the result of either changes in the radiation field (which should be fully determined by A_V) or grain growth (which would change R_V). However, these data do fall within the range for which our modeled values of $\lambda_{\max}$ are most efficiently varied by changing the volume density—the data are effectively bounded by models with densities (0.1 to $40) \times 10^3 \, \text{cm}^{-3}$ (Figure 5d). Thus the dispersion is most likely a result of an increased gas-grain collision rate which causes an increase in $b_{\min}$. Given the low average density in the cloud ($\sim 1 \times 10^3 \, \text{cm}^{-3}$; Blitz & Williams 1997) the areas of higher collision may result from higher-density clumps along these lines of sight, especially at $A_V < 0.8$ mag where the low extinction would indicate lower volume densities than the $A_V = 1.5$–2.5 mag sample.

4.5. *Comparison of Models Data*

Between $A_V \sim 1$ and 6 mag, model 2 (red line in Figure 5d) reproduces the observed linear relationship in the lower-branch data (grey, solid, curve in Figures 5a–b), before flattening out beyond $A_V \sim 10$ mag. This flat part of the curve results from a lack of grains beyond the upper-size cut-off of 0.3 μm that satisfy the RAT alignment condition ($a > 2\lambda$) for the remaining, reddened, radiation field. To reach the measured values for Elias 3-16 ($A_V = 24.1$ mag, $\lambda_{\max} = 1.08 \, \mu\text{m}$) we increased the largest grain size to $b_{\max} = 0.5 \, \mu\text{m}$ (model 3). This new curve only deviates from the baseline model beyond $A_V \approx 6$ mag, confirming that these values of $b_{\max}$ do not strongly influence the results at low extinction.

To reproduce the upper branch data, in which $\lambda_{\max} > 0.8 \, \mu\text{m}$ above 6 mag, it was necessary to increase both the size of largest grains in the model and the gas density. The resulting increase in $b_{\min}$ due to collisions, together with the larger value of $b_{\max}$, increases the average size of aligned grains, and hence increases $\lambda_{\max}$ significantly. Models 4–6 yield equivalent $\lambda_{\max}$ at low extinction because they all use the same volume density ($4 \times 10^4 \, \text{cm}^{-3}$), but increase to larger values of $\lambda_{\max}$ as $b_{\max}$ increases. Model 7 with $b_{\max} = 0.7 \, \mu\text{m}$ yields the best match to the upper branch data (Figure 5d).

Grain growth in dense clouds is thought to be dominated by grain coagulation (Ormel et al. 2009), which is a collisional process. This is especially so for the silicates (Hirashita & Voshchinnikov 2014), which are responsible for polarization. The upper-branch models require both enhanced gas densities and increases in $a_{\max}(= b_{\max})$, neither change alone is sufficient. Such a correlation of increased gas density and larger grain sizes is expected for models of grain growth through co-

Table 8. Parameters of Grain Alignment Models

Model Number	Gas Density (10^3 cm^{-3})	b_{max} (μm)	$\lambda_{max}(0)$[a] (μm)	Figure Legend[b]	
1	0.1	0.3	0.49	solid,	black
2	10	0.3	0.55	solid,	red
3	10	0.5	0.55	dotted,	red
4	40	0.3	0.65	solid,	blue
5	40	0.6	0.65	dashed,	blue
6	40	0.7	0.65	solid,	green

NOTE—All models have a gas temperature of 20 K.

[a] Limit as extinction approaches zero; $b_{min} = a_{min}$.

[b] Line color and type used in Figures 5c–d.

agulation. Therefore, the bifurcation of the λ_{max} vs. A_V relationship into two branches may indicate the presence of a clumpy volume density structure, and possibly fractal cloud structures (Falgarone et al. 1991; Falgarone & Phillips 1996) where, even for high-A_V regions, only some lines of sight probe dense material with significant grain growth. Note that the strong bifurcation between the two branches suggests that any given sight line is dominated by either strong grain growth (the upper branch with $a_{max} = 0.7\,\mu$m) or only moderate growth (the lower branch with $a_{max} < 0.5\,\mu$m). Otherwise one would expect more points to fall between the two branches. Polarization spectra of additional stars at high extinction are needed to sample the region between the branches.

Based on scattering theory one expects that both λ_{max} and R_V depend on grain size and, thus, that the two parameters are correlated. We used Gaia photometric data to estimate the total-to-selective extinction ratio towards the SWIW sample using two methods: 1) using the equation $R_V = 1.1 \cdot E_{V-K}/E_{B-V}$ (Whittet & van Breda 1978); and 2) by fitting a second order polynomial to $E_{\lambda-V}/E_{B-V}$ as a function of $1/\lambda$ and finding $R_V = \lim_{\lambda \to \infty} E_{\lambda-V}/E_{B-V}$ (c.f., Whittet 2003). The results from the two methods, shown in Table 2, generally agree well. (We found that fits based on color-transformed SDSS or Pan-STARRS (e.g. Jester et al. 2005) data tended to yield extreme, and often un-physical results and have, therefore, used the AAVSO (B,V) data where available.)

Values for λ_{max} and R_V for the high-density sample are compared in Figure 6. While a significant number of outliers are apparent in this plot, a weak correlation is apparent in the central part ($\lambda_{max} = 0.55–0.90\,\mu$m, $R_V = 2–6$). The upper-branch stars (labeled "U" in the figure) show both larger λ_{max} and slightly larger R_V from the lower-branch (unlabeled) stars. Given the many uncertainties associated with calculating R_V for these stars (e.g., spectral class assignments affecting the intrinsic colors, emission lines affecting the observed colors), as well as small-number statistics it is not surprising that the apparent correlation between λ_{max} and R_V is small in our sample. Because λ_{max} is not affected by the above stellar and photo-metric uncertainties, we expect that it is a more direct measure of the average grain size along the line of sight than is R_V.

5. CONCLUSIONS

We have acquired and analyzed an expanded sample of multi-band photo-polarimetry at moderate extinctions (62 stars), and visible spectro-polarimetry of high-extinction lines of sight (25 stars), through the Taurus cloud complex. To the visible spectropolarimetry data, we add NIR H-band polarimetry in order to better constrain polarization vs. wavelength fits to the Serkowski relation parameters (p_{max}, λ_{max}, K).

We confirm the previously established (Whittet et al. 2001; Andersson & Potter 2007) correlation between λ_{max} and A_V for extinctions up to $A_V \approx 4$ mag. Beyond ~4 mag, the λ_{max} vs. A_V relationship bifurcates, with part of the sample continuing the previously observed relation (a "lower branch") while another part of the sample has a significantly steeper dependence of λ_{max} on A_V (an "upper branch").

Using RAT modeling of the grain alignment and radiative transfer in the cloud, we find that the lower branch data are well modeled by RAT alignment of grains with a fixed size distribution, illuminated by an increasingly reddened diffuse interstellar radiation field, and a constant level of gas-grain collisional disalignment. For lines of sight having $A_V = 1.5–2.5$ mag and enhanced λ_{max} values, increased collisional disalignment alone can explain the observed behavior, consistent with the lack of an increase in the total-to-selective extinction (R_V) for these lines of sight.

For the upper branch, both grain growth and increased collisional disalignment of the smallest grains are required to match the observations (c.f., Whittet 2003). That the grain growth on the upper branch is associated with enhanced volume density is consistent with the expectation that grain growth through coagulation is a collisional process, and therefore will proceed faster in denser material.

Our results indicate that multi-band polarization can be used as a new tool to probe grain growth in molecular clouds, independent of assumptions about grain temperature and emissivity required for the combination of near- and far-infrared data (Ysard et al. 2013).
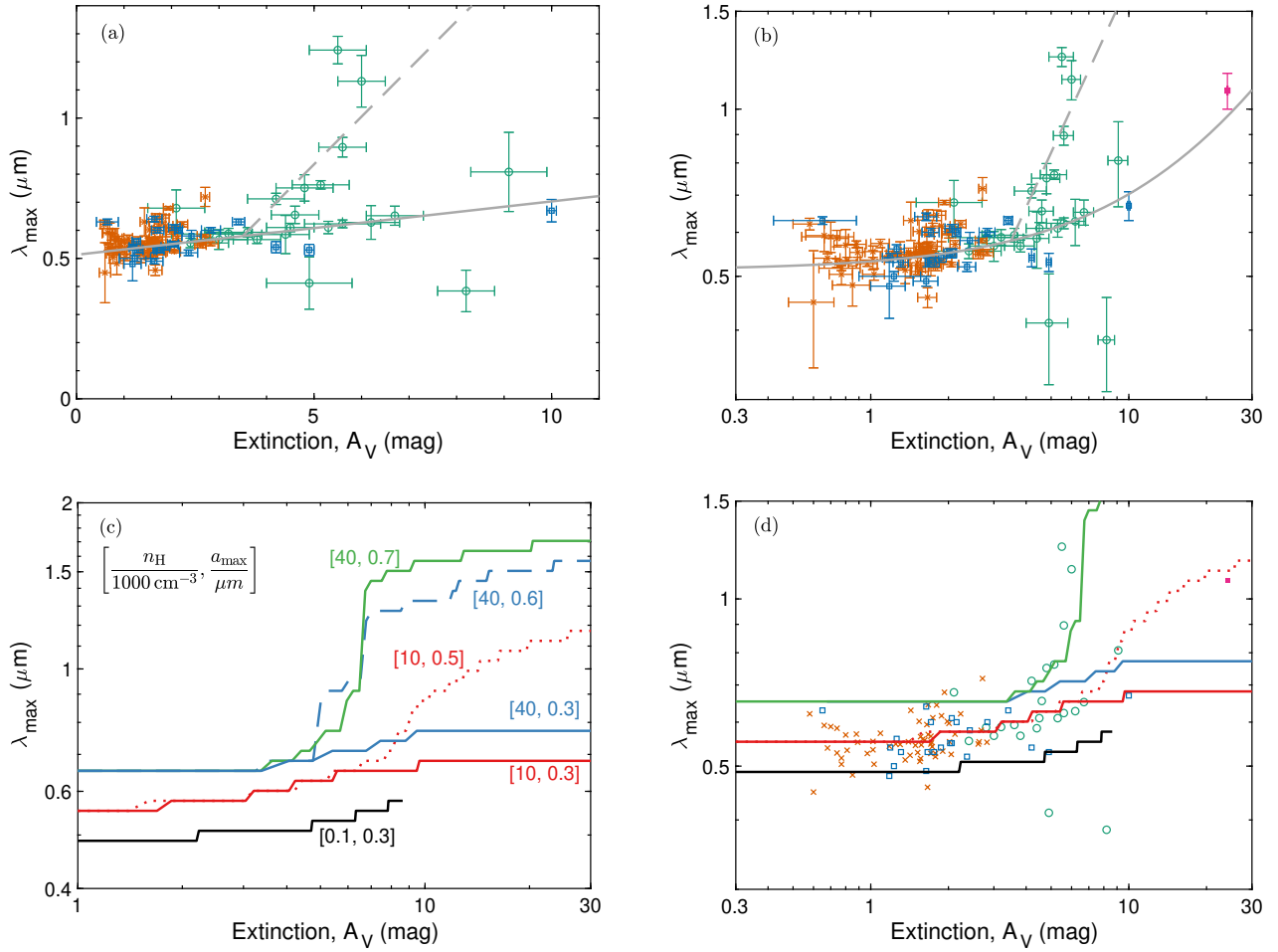
Figure 5. Panels (*a*) and (*b*) show the relation between the wavelength peak of the polarization curve ($\lambda_{\max}$; equation [1]) and optical extinction (A_V) towards stars behind Taurus. Data are from both this work (Kast/Lick = green and TurPol/NOT = orange) and Whittet et al. (2001; blue). Panel (*a*) is plotted using linear axes while panel (*b*) is plotted logarithmically and also includes the data point for Elias 3-16 (Hough et al. 1988; Murakawa et al. 2000; magenta). The solid and dashed lines show the best linear fits to the "upper" and "lower" branches (Table 7), respectively. (*c*) Model fits based on RAT alignment are shown for a number of model parameters. Lines are labeled with the volume density (in units of $1000\,\mathrm{cm}^{-3}$) and the maximum grain size (μm) in each model. In order to show the key model differences, the plot shows a slightly different range of A_V and $\lambda_{\max}$ from panels *a*, *b*, and *d*. Panel (*d*) compares several of the models in panel *c* (using the same color scheme) with the data in panels *a* and *b*. The error bars on the data are removed for clarity only.

Figure 6. Extinction ratio and λ_{max}. The total-to-selective extinction ratio (R_V) for the SWIW sample is plotted with the measured values of λ_{max}. The blue circles represent values derived from the relation $R_V = 1.1 \cdot E_{V-K}/E_{B-V}$ (Whittet & van Breda 1978), while the red triangles represent values derived from $R_V = \lim_{\lambda \to \infty} E_{\lambda-V}/E_{B-V}$ (c.f. Whittet 2003). Stars on the upper branch of Figure 5 are labeled as "U", while lower branch stars remain unlabeled.

APPENDIX

A. DATA REDUCTION FOR OPTICAL SPECTROPOLARIMETRY

This appendix discusses details of the polarization analyses performed on the data collected with the Kast spectropolarimeter on the 3 m Shane telescope of Lick Observatory (Section 2.3; Miller et al. 1988).

A.1. *The Polarization Signal*

The spectral images for all stars and standards were flat-fielded at each of the eight HWP angles. Spectra of the two orthogonal polarizations (the ordinary, O, and extraordinary, E, rays) were separately wavelength-calibrated and extracted using standard IRAF[3] routines in the APEXTRACT package.

Given the extraordinary $E(\lambda, \theta)$ and ordinary $O(\lambda, \theta)$ spectral signals, at HWP angle θ and wavelength λ, we defined the difference and sum (Stokes I) signals as

$$d(\lambda, \theta) \equiv O(\lambda, \theta) - E(\lambda, \theta) \tag{A1}$$

$$\text{and} \quad I(\lambda, \theta) \equiv O(\lambda, \theta) + E(\lambda, \theta). \tag{A2}$$

The polarization signal is then

$$S(\lambda, \theta) = \frac{d(\lambda, \theta)}{I(\lambda, \theta)}. \tag{A3}$$

For an ideal HWP, this signal has the form

$$S(\lambda, \theta, \delta) = a(\lambda) + p(\lambda) \cos 4[\theta - \delta(\lambda)] \tag{A4}$$

$$= a(\lambda) + q(\lambda) \cos 4\theta + u(\lambda) \sin 4\theta \tag{A5}$$

---

[3] IRAF is distributed by the National Optical Astronomy Observatories, which are operated by the Association of Universities for Research in Astronomy, Inc., under cooperative agreement with the National Science Foundation. (http://iraf.noao.edu/)

where (dropping the λ-dependence for simplicity) p is the polarized fraction, δ is the phase angle of the measured polarization, and q and u are the reduced-Stokes parameters, $q \equiv Q/I = p \cos 4\delta$ and $u \equiv U/I = p \sin 4\delta$. The offset factor a accounts for gain differences (between the E- and O-beams of the Wollaston prism) that have not been completely corrected by the flat-fielding analysis step (e.g., Patat et al. 2006). Note that I is the total intensity Stokes parameter and is, ideally, equivalent to that in equation (A2) and expected to have no θ-dependence. The phase angle and polarization are related to the Stokes parameters via

$$p = \left(q^2 + u^2\right)^{1/2} \tag{A6}$$

$$\text{and} \quad 2\delta = \frac{1}{2} \arctan\left(\frac{u}{q}\right), \tag{A7}$$

where we have again dropped the λ-dependence on all four parameters. The polarization angle in space, 2δ, is related to the stellar polarization position angle θ projected onto the sky and several instrument parameters (see Appendix B.3).

To improve the signal-to-noise on individual measurements, the spectra for the sum $I(\lambda, \theta)$ and difference $d(\lambda, \theta)$ signals in the 0.460–1.010 μm range were averaged into 11 bins, each 0.050 μm wide, with equal weighting applied to all spectral pixels in a bin. Nominally, the uncertainty in each bin would be the standard deviation of the mean. However, as described in Section 2, the spectral resolution of our observations was typically 3–5 on-chip pixels FWHM ($\approx 0.0020 \, \mu$m), so that the individual pixels in an averaged bin were not statistically independent. To correct for this, the uncertainty on the difference signal in each 0.050 μm bin was set to twice the standard deviation of the mean. The uncertainty on the sum signal at every θ was taken to be the standard deviation of the measurements across all eight HWP angles. Since the intensity $I(\lambda, \theta)$ was nominally independent of HWP angle θ, its repeatability was used as an estimate of the measurement uncertainty. This variation is most likely the result of a time-variable sky transmission which we have not attempted to remove here (e.g., Clemens et al. 2012a). The uncertainties on the sum and difference signal were propagated into those for the polarization signal $S(\theta, \lambda)$.

Empirically, the different uncertainties for I and d at each HWP angle in a given wavelength bin were comparable. Occasionally some uncertainty values did differ significantly, which was not unexpected given the large data set. To avoid over- or under-weighting these data in the fits, we assign uniform uncertainties $\sigma_u(\lambda)$ to the polarization signals $S(\lambda, \theta)$ within each wavelength bin. Within each wavelength bin, the uniform uncertainties are given by the median uncertainty across the HWP angles θ_i in that bin, such that $\sigma(\lambda, \theta_i) = \sigma_u(\lambda) = \text{median}[\sigma(\lambda, \theta_i)]$.

A.2. *Polarization Fits*

Equation (A5) describes a set of coupled linear equations whose solution is found by performing a standard linear regression. That is, we wish to solve the coupled equations

$$S = \mathbf{A}x, \tag{A8}$$

where the data vector is

$$S(\lambda) = \begin{bmatrix} S(\theta_1, \lambda) \\ \vdots \\ S(\theta_n, \lambda) \end{bmatrix} \tag{A9}$$

and n is the number of HWP angles (typically $n = 8$). The parameter matrix with the fit Stokes parameters is

$$x(\lambda) = \begin{bmatrix} a(\lambda) \\ q(\lambda) \\ u(\lambda) \end{bmatrix}, \tag{A10}$$

$$\mathbf{A} = \begin{bmatrix} 1 & \cos 4\theta_1 & \sin 4\theta_1 \\ \vdots & \vdots & \vdots \\ 1 & \cos 4\theta_n & \sin 4\theta_n \end{bmatrix}. \tag{A11}$$

The least-squares solution to equation (A8) is

$$\tilde{x} = \left(\mathbf{A}^{\mathrm{T}} \Sigma^2 \mathbf{A}\right)^{-1} \mathbf{A}^{\mathrm{T}} \Sigma^2 S. \tag{A12}$$

where the matrix of inverse-variances is diagonal with elements $\Sigma_{ii}^2 = \left[1/\sigma(\theta_i, \lambda)\right]^2$.

Parameter uncertainties follow from the diagonal elements of the covariance matrix such that

$$\left(\mathbf{A}^{\mathrm{T}} \Sigma^2 \mathbf{A}\right)^{-1} = \sigma^2(\lambda) \left[\mathbf{A}^{\mathrm{T}}\mathbf{A}\right]^{-1} = \begin{bmatrix} \sigma_{aa}^2 & \sigma_{aq}^2 & \sigma_{au}^2 \\ \sigma_{aq}^2 & \sigma_{qq}^2 & \sigma_{qu}^2 \\ \sigma_{au}^2 & \sigma_{qu}^2 & \sigma_{uu}^2 \end{bmatrix}, \tag{A13}$$
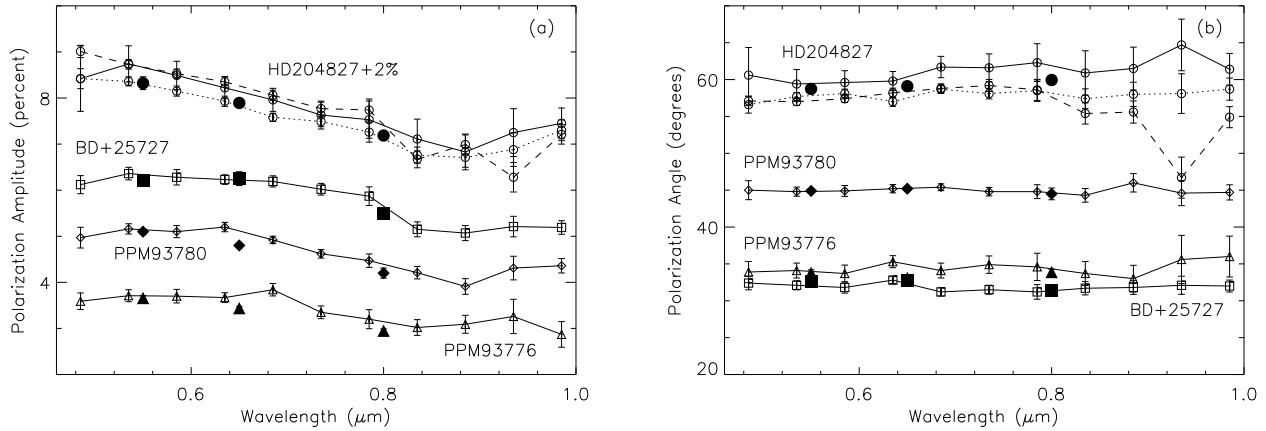
Figure 7. Polarization amplitudes (*a*) and angles (*b*) measured for standard high-polarization stars (see Table 9). All three separate measurements for HD 204827 are shown as open circles with different observations indicated by different line-types. Error-bars represent only the statistical uncertainties in the polarization fits and do not include any estimate of systematic uncertainties. Large solid symbols show TurPol measurements of all four stars through broadband *V* (0.55 μm), *R* (0.65 μm), and *I* (0.80 μm) filters (see text for references and band definitions). Uncertainties for data without error-bars are smaller than the plotted symbols. For clarity, the polarization amplitude data for HD 204827 have been shifted up by 2%.

where the first equality holds when the uncertainties are the same for all HWP angles. For the typical case with eight equally spaced HWP angles from zero to 157.5, degrees all off-diagonal terms reduce to zero and the diagonal terms simplify to $\sigma_{aa}(\lambda) = \sigma(\lambda)/\sqrt{8}$ and $\sigma_{qq}(\lambda) = \sigma_{uu}(\lambda) = \sigma(\lambda)/2$.

The least-squared solutions also return reduced-χ^2 goodness-of-fit parameters for each wavelength bin for each star. Of the 275 fitted data points (11 wavelengths × 25 stars) the returned χ^2 values have a log-normal distribution with median 0.55 and standard deviation 0.7.

The polarization amplitude, polarization phase angle, and their respective uncertainties follow from equations (A6) and (A7). Note that some measurements did not include all eight HWP angles. For those objects the off-diagonal covariance terms cannot necessarily be ignored and must be included when calculating the amplitude and phase uncertainties. However, in practice we found that the covariance terms were much smaller than the diagonal terms for our particular dataset and so did not include them in the calculation.

B. POLARIZATION CALIBRATION FOR OPTICAL SPECTROPOLARIMETRY

B.1. *Polarization Standards*

Table 9 lists observations of several known high-polarization stars[4] (Schmidt et al. 1992; Turnshek et al. 1990). We used these observations as a check against systematic errors introduced via the observations with the Kast spectropolarimeter or the data analysis process, and to calibrate the angular position of the Kast instrument. Two stars were used throughout the three nights of observations, with BD+25727 observed only on the first night and HD 204827 on all three nights. Polarization results for all 11 passbands are given in Figure 7 and Table 9. For comparison, we also plot the broadband measurements from the literature for HD 204827 (Schmidt et al. 1992), results from the Nordic Optical telescope for BD+25727[5], and the results of our TurPol observations for the stars PPM 93776 and PPM 93780.

The star HD 212311 was observed as a standard unpolarized star (Turnshek et al. 1990) during all three nights of observations. Due to the low level of instrument polarization, there was insufficient signal-to-noise to measure it independently in each wavelength bin. Averaging the fit Stokes parameters across all wavelength bins yielded 0.1%–0.3%, consistent with other calibrations of the Kast spectropolarimeter (Ryan Chornock 2010, private communication; Leonard et al. 2001; Chornock et al. 2010; Eswaraiah et al. 2012). The star PPM 93241 was used as a secondary unpolarized standard based on our more precise TurPol results for that star (Table 3). Measured Kast values are also 0.1%–0.3%, compared to the TurPol results that average ∼0.1%–0.2%. Since these low levels of instrument polarization are comparable to the statistical and systematic uncertainties in the Kast data, we made no correction for the instrument polarization.

To facilitate quantitative comparison with the broadband observations, we define *V*-, *R*-, and *I*-like passbands for the Kast spectra with centers at 0.55, 0.65, and 0.80 μm, with widths of 0.10, 0.10, and 0.15 μm, respectively, and uniform responses across those widths. The results for the standard stars in these passbands are given in Table 9. The angle values are in good agreement, within the statistical uncertainties on the measurements and the angle calibration (a total of ∼1.5°–2°; Appendix B.3). With the exception of an

---

[4] http://www.not.iac.es/instruments/turpol/std/hpstd.html

[5] http://www.not.iac.es/instruments/turpol/std/bd25727_note.html

Table 9. Standard High-polarization Stars observed using Kast

Object	Band	Center Wavelength[a]		q	σ_q	u	σ_u	p	σ_p	θ[b]	σ_θ	χ_r^2
			(μm)	(%)	(%)	(%)	(%)	(%)	(%)	(deg.)	(deg.)	
BD +25727	Narrow		0.485	2.44	0.20	5.61	0.20	6.12	0.20	33.2	0.9	2.00
BD +25727	Narrow		0.535	2.60	0.14	5.81	0.14	6.36	0.14	32.9	0.6	0.45
...	...	...	...	...	...	...	...	...	...	...	...	...
HD 204827 (n2)[c]	"V"		0.550	−2.83	0.14	4.88	0.14	5.63	0.14	60.1	0.7	6.60
HD 204827 (n2)[c]	"R"		0.650	−2.77	0.10	4.34	0.10	5.14	0.10	61.3	0.6	12.0
HD 204827 (n2)[c]	"I"		0.800	−2.48	0.16	3.61	0.16	4.38	0.16	62.2	1.1	2.40
...	...	...	...	...	...	...	...	...	...	...	...	...

[a] Data are reported in 11 wavelength bins with centers spanning 0.485–0.985 μm with widths of 0.050 μm ("Narrow"). Also shown are data in three bins with centers 0.550, 0.650, and 0.800 μm with full-widths of 0.100, 0.100, and 0.150 μm, respectively; we refer to these as the V-, R-, and I-like broadband filters.

[b] Polarization position angle measured east of north.

[c] Data for HD 204827 are given for three separate nights of observations labeled n2, n3, and n4.

NOTE—All polarization data for the standard high-polarization stars used here. Listed uncertainties are statistical only and are returned as part of the fitting procedure, along with the reduced-χ^2 reported in the last column; uncertainties here do not include other systematics discussed in the text. (This table is available in its entirety in a machine-readable form in the online journal. A portion is shown here for guidance regarding its form and content.)

outlier in one measurement of HD 204827 (night-4, 0.935 μm), these stellar data are all consistent with wavelength-independent position angles. Absolute deviations of the measured polarization amplitudes from their "expected" values are in the 0.0%–0.4% range. We attribute this level of deviation to contributions from the statistical uncertainties (0.1%–0.2%) and the instrument polarization (0.1%–0.3%).

B.2. *Polarization Efficiency*

To measure the polarization efficiency of the Kast instrument, a polarizing filter is inserted just before the HWP (Miller et al. 1988). Standard polarization measurements are then performed using known standard unpolarized stars to illuminate the slit. Over the course of three nights we obtained data using four separate observations of PPM 93241 and three observations of HD 212311. These seven observations were treated as independent observations and reduced as described in Appendix A.2. In the range 0.460–0.860 μm the median efficiencies are 99.7%–99.9%; the standard deviation across the seven measurements is $\lesssim$0.1%. Beyond 0.860 μm the efficiency drops rapidly, reaching about 50% by 1.000 μm. This sharp drop was not seen in any of the standard high-polarization stars we observed (Section B.1). Therefore, we attribute this drop not to any down-stream optical element in the instrument, but to the polarizing filter itself. This is consistent with work by other users of the Kast polarimeter (Ryan Chornuck, private communication; Miller et al. 1988). Given measurements of such high efficiency, we made no corrections in any of the polarization measurements made herein.

B.3. *Polarization Angle Calibration*

The polarization position angle θ of a celestial source projected on the sky is related to the measured HWP phase angle 2δ (equation [A7]), the rotation angle of the instrument, γ, and the orientation of the HWP's fast and slow axes, χ, via the relation

$$\theta(\lambda) = \gamma - 2\delta(\lambda) + \chi(\lambda) - \beta. \tag{B14}$$

The instrument rotation angle γ is the angle of an instrument axis measured east of north. The "zero-angle" of the HWP, $\chi(\lambda)$, was measured by inserting a polarizing filter into the optical path. This quantity measures the angle with respect to the linearly polarizing axis of this filter. The angle β describes the remaining angle between the instrument axis which defines γ and the axis of the polarizing grid; this was measured by comparing the measured angles with those of standard high-polarization stars.

When the polarizing filter was in place, we set $\theta = \gamma = \beta = 0$ in equation (B14) yielding $\chi(\lambda) = 2\delta(\lambda)$. This angle varied by nearly $5°$ across the 0.460–1.000 μm range. The trend in wavelength was consistent across different measurements with relative offsets as large as $\sim$0.3°. This offset was consistent with the repeatability of placing either the HWP or the polarizing filter at any given angular position (Miller et al. 1988). Therefore, we assigned a $\sim$0.3° systematic uncertainty to all angle analyses in this work.

To correct for the wavelength dependence of the phase angle, we used the median angles that resulted after shifting all angles to agree at *R*-band; we set this value to zero degrees at *R*-band. To check this correction, we examined the residuals after subtracting the median angles from the shifted observations. The variation across wavelengths, which was previously as large as $5°$, was reduced to $\lesssim$0.3°.

In order to measure β, we used the angles measured in the synthetic broadband *V*-, *R*-, and *I*-like filters (corrected for the instrument angle γ and the wavelength-dependent HWP-zero angle χ) for BD+25727 and HD 204827 and compared them to previous measurements of those same stars. These three filters and two stars resulted in 12 separate measurements of β with a median of $-96.8°$ and a standard deviation of 1.3°. The measured angles in Tables 4 and 9 were corrected using this value. Quadratically combining the angle uncertainties from the fitted data, uncertainties in HWP-zero angle ($\sim$0.3°), and the uncertainty on β reported here yielded typical angle uncertainties $\sim$1.5°–2°. These uncertainty estimates were consistent with the repeatability of the HD 204827 angle estimates. Additionally, the resulting broadband angles were in good agreement with the TurPol data for PPM 93776 and PPM 93780.

C. SERKOWSKI & WILKING FITS

The polarization-wavelength relation in equation (1) can be written as a polynomial that is linear in its coefficients (e.g., Coyne et al. 1974):

$$\ln p = X_1 + X_2 \ln \lambda - K \ln^2 \lambda, \tag{C15}$$

where

$$X_1 = \ln p_{\max} - K \ln^2 \lambda_{\max}, \tag{C16}$$

$$X_2 = 2K \ln \lambda_{\max}. \tag{C17}$$

The solution for the coefficients X_1, X_2, and K is a linear regression, similar to that in Section A.2. The values $p_{\max}$ and $\lambda_{\max}$ are then found from equations (C16)–(C17).

The reduced-χ^2 values in Tables 5 and 6 utilize the fits to equation (C15). This applies to both the Kast and Turpol data.

REFERENCES

Adolfsson, T. 1954, Arkiv for Astronomi, 1, 425

Akimoto, H., & Itoh, Y. 2019, International Journal of Astronomy and Astrophysics, 9, 321, doi: 10.4236/ijaa.2019.93023

Andersson, B-G 2015, in Astrophysics and Space Science Library, Vol. 407, Magnetic Fields in Diffuse Media, ed. A. Lazarian, E. M. de Gouveia Dal Pino, & C. Melioli, 59

Andersson, B-G, Lazarian, A., & Vaillancourt, J. E. 2015, ARA&A, 53, 501, doi: 10.1146/annurev-astro-082214-122414

Andersson, B-G, & Potter, S. B. 2007, ApJ, 665, 369, doi: 10.1086/519755

Bailer-Jones, C. A. L., Rybizki, J., Fouesneau, M., Mantelet, G., & Andrae, R. 2018, AJ, 156, 58, doi: 10.3847/1538-3881/aacb21

Bayo, A., Rodrigo, C., Barrado Y Navascués, D., et al. 2008, A&A, 492, 277, doi: 10.1051/0004-6361:200810395

Bevington, P. R., & Robinson, D. K. 1992, Data reduction and error analysis for the physical sciences (New York: McGraw-Hill, |c1992, 2nd ed.)

Blitz, L., & Williams, J. P. 1997, ApJL, 488, L145, doi: 10.1086/310941

Cardelli, J. A., Clayton, G. C., & Mathis, J. S. 1988, ApJL, 329, L33, doi: 10.1086/185171

Chandrasekhar, S., & Fermi, E. 1953, ApJ, 118, 113

Chornock, R., Filippenko, A. V., Li, W., & Silverman, J. M. 2010, ApJ, 713, 1363, doi: 10.1088/0004-637X/713/2/1363

Cizdziel, P. J. 1990, in Astronomical Society of the Pacific Conference Series, Vol. 8, CCDs in astronomy, ed. G. H. Jacoby, 100–110

Clayton, G. C., Wolff, M. J., Sofia, U. J., Gordon, K. D., & Misselt, K. A. 2003, ApJ, 588, 871

Clemens, D. P., Pinnick, A. P., & Pavel, M. D. 2012a, ApJS

Clemens, D. P., Pinnick, A. P., Pavel, M. D., & Taylor, B. 2012b, ApJS

Clemens, D. P., Sarcia, D., Grabau, A., et al. 2007, PASP, 119, 1385, doi: 10.1086/524775

Coelho, P. R. T. 2014, MNRAS, 440, 1027, doi: 10.1093/mnras/stu365

Cohen, M., & Kuhi, L. V. 1979, ApJS, 41, 743, doi: 10.1086/190641

Coyne, G. V., Gehrels, T., & Serkowski, K. 1974, AJ, 79, 581

Cudlip, W., Furniss, I., King, K. J., & Jennings, R. E. 1982, MNRAS, 200, 1169, doi: 10.1093/mnras/200.4.1169

Davis, L. 1951, Physical Review, 81, 890, doi: 10.1103/PhysRev.81.890.2

Davis, L. J., & Greenstein, J. L. 1951, ApJ, 114, 206

Dotson, J. L., Davidson, J., Dowell, C. D., Schleuning, D. A., & Hildebrand, R. H. 2000, ApJS, 128, 335, doi: 10.1086/313384

Draine, B. T., & Lazarian, A. 1998, ApJ, 508, 157, doi: 10.1086/306387

Draine, B. T., & Weingartner, J. C. 1996, ApJ, 470, 551, doi: 10.1086/177887

—. 1997, ApJ, 480, 633, doi: 10.1086/304008

Eswaraiah, C., Pandey, A. K., Maheswar, G., et al. 2012, MNRAS, 419, 2587, doi: 10.1111/j.1365-2966.2011.19908.x

Falgarone, E., & Phillips, T. G. 1996, ApJ, 472, 191, doi: 10.1086/178054

Falgarone, E., Phillips, T. G., & Walker, C. K. 1991, ApJ, 378, 186

Fosalba, P., Lazarian, A., Prunet, S., & Tauber, J. A. 2002, in American Institute of Physics Conference Series, Vol. 609, Astrophysical Polarized Backgrounds, ed. S. Cecchini, S. Cortiglioni, R. Sault, & C. Sbarra, 44–50

Gaia Collaboration, Brown, A. G. A., Vallenari, A., et al. 2018, A&A, 616, A1, doi: 10.1051/0004-6361/201833051

Galli, P. A. B., Loinard, L., Bouy, H., et al. 2019, A&A, 630, A137, doi: 10.1051/0004-6361/201935928

Gold, T. 1952, MNRAS, 112, 215

Hall, J. S. 1949, Science, 109, 166

Henden, A. A., Templeton, M., Terrell, D., et al. 2016, VizieR Online Data Catalog, II/336

Herbig, G. H., & Bell, K. R. 1988a, Third Catalog of Emission-Line Stars of the Orion Population : 3 : 1988

—. 1988b, Lick Observatory Bulletin, Vol. 1111, Third Catalog of Emission-Line Stars of the Orion Population

Herczeg, G. J., & Hillenbrand, L. A. 2014, ApJ, 786, 97, doi: 10.1088/0004-637X/786/2/97

Hildebrand, R. H. 1988, QJRAS, 29, 327

Hiltner, W. A. 1949a, Science, 109, 165

—. 1949b, ApJ, 109, 471

Hirashita, H., & Voshchinnikov, N. V. 2014, MNRAS, 437, 1636

Hoang, T., & Lazarian, A. 2008, MNRAS, 388, 117, doi: 10.1111/j.1365-2966.2008.13249.x

—. 2016, ApJ, 821, 91

Hoang, T., Lazarian, A., & Andersson, B-G. 2015, MNRAS, 448, 1178, doi: 10.1093/mnras/stu2758

Høg, E., Fabricius, C., Makarov, V. V., et al. 2000, A&A, 355, L27

Hough, J. H., Aitken, D. K., Whittet, D. C. B., Adamson, A. J., & Chrysostomou, A. 2008, MNRAS, 387, 797, doi: 10.1111/j.1365-2966.2008.13274.x

Hough, J. H., Sato, S., Tamura, M., et al. 1988, MNRAS, 230, 107

Jacoby, G. H., Hunter, D. A., & Christian, C. A. 1984, ApJS, 56, 257, doi: 10.1086/190983

Jester, S., Schneider, D. P., Richards, G. T., et al. 2005, AJ, 130, 873, doi: 10.1086/432466

Jones, T. J. 1989, ApJ, 346, 728, doi: 10.1086/168054

Kenyon, S. J., Gomez, M., Marzke, R. O., & Hartmann, L. 1994, AJ, 108, 251, doi: 10.1086/117064

Kenyon, S. J., Gómez, M., & Whitney, B. A. 2008, in ASP Monograph, Vol. 4, Handbook of Star Forming Regions, Volume I: The Northern Sky, ed. B. Reipurth (ASP), 405

Kim, S.-H., & Martin, P. G. 1995, ApJ, 444, 293, doi: 10.1086/175604

Lazarian, A., Andersson, B-G, & Hoang, T. 2015, Grain Alignment: Role of Radiative Torques and Paramagnetic Relaxation; L. Kolokolova, J. Hough and A.-C. Levasseur-Regourd eds. (Cambridge: University Press, 2015), 81–113

Lazarian, A., & Draine, B. T. 1999, ApJL, 516, L37, doi: 10.1086/311986

Lazarian, A., & Hoang, T. 2007, MNRAS, 378, 910, doi: 10.1111/j.1365-2966.2007.11817.x

Leonard, D. C., Filippenko, A. V., Ardila, D. R., & Brotherton, M. S. 2001, ApJ, 553, 861, doi: 10.1086/320959

Luhman, K. L., Mamajek, E. E., Allen, P. R., & Cruz, K. L. 2009, ApJ, 703, 399, doi: 10.1088/0004-637X/703/1/399

Martin, P. G. 1974, ApJ, 187, 461, doi: 10.1086/152655

Mathis, J. S. 1986, ApJ, 308, 281, doi: 10.1086/164499

Mathis, J. S., Mezger, P. G., & Panagia, N. 1983, A&A, 128, 212

Mathis, J. S., Rumpl, W., & Nordsieck, K. H. 1977, ApJ, 217, 425

Medan, I., & Andersson, B-G. 2019, ApJ, 873, 87, doi: 10.3847/1538-4357/ab063c

Miller, J. S., Robinson, L. B., & Goodrich, R. W. 1988, in Instrumentation for Ground-Based Optical Astronomy, ed. L. B. Robinson, 157

Murakawa, K., Tamura, M., & Nagata, T. 2000, ApJS, 128, 603, doi: 10.1086/313387

Nozawa, T. 2016, Planet. Space Sci., 133, 36, doi: 10.1016/j.pss.2016.08.006

Ormel, C. W., Paszun, D., Dominik, C., & Tielens, A. G. G. M. 2009, A&A, 502, 845, doi: 10.1051/0004-6361/200811158

Page, L., Hinshaw, G., Komatsu, E., et al. 2007, ApJS, 170, 335, doi: 10.1086/513699

Patat, F., Benetti, S., Cappellaro, E., & Turatto, M. 2006, MNRAS, 369, 1949, doi: 10.1111/j.1365-2966.2006.10451.x

Piirola, V. 1988, Simultaneous five-colour (UBVRI) photopolarimeter (Polarized Radiation of Circumstellar Origin), 735–746

Planck Collaboration, Aghanim, N., Akrami, Y., et al. 2018, arXiv e-prints, arXiv:1807.06207. https://arxiv.org/abs/1807.06207

Purcell, E. M. 1976, ApJ, 206, 685

Rebull, L. M., Padgett, D. L., McCabe, C. E., et al. 2010, ApJS, 186, 259, doi: 10.1088/0067-0049/186/2/259

Rebull, L. M., Koenig, X. P., Padgett, D. L., et al. 2011, ApJS, 196, 4, doi: 10.1088/0067-0049/196/1/4

Romano, G. 1975, Mem. Soc. Astron. Italiana, 46, 81

Scarrott, S. M., Ward-Thompson, D., & Warren-Smith, R. F. 1987, MNRAS, 224, 299, doi: 10.1093/mnras/224.2.299

Schmidt, G. D., Elston, R., & Lupie, O. L. 1992, AJ, 104, 1563, doi: 10.1086/116341

Serkowski, K. 1968, ApJ, 154, 115

Serkowski, K., Mathewson, D. L., & Ford, V. L. 1975, ApJ, 196, 261

Shenoy, S. S., Whittet, D. C. B., Ives, J. A., & Watson, D. M. 2008, ApJS, 176, 457, doi: 10.1086/533532

Simmons, J. F. L., & Stewart, B. G. 1985, A&A, 142, 100

Skrutskie, M. F., Cutri, R. M., Stiening, R., et al. 2006, AJ, 131, 1163, doi: 10.1086/498708

Spitzer, L., & Tukey, J. W. 1949, Science, 109, 461, doi: 10.1126/science.109.2836.461

Spoelstra, T. A. T. 1984, A&A, 135, 238

Tamura, M., Nagata, T., Sato, S., & Tanaka, M. 1987, MNRAS, 224, 413, doi: 10.1093/mnras/224.2.413

Teixeira, T. C., & Emerson, J. P. 1999, A&A, 351, 292

Turnshek, D. A., Bohlin, R. C., Williamson, R. L., et al. 1990, AJ, 99, 1243, doi: 10.1086/115413

Vaillancourt, J. E. 2006, PASP, 118, 1340, doi: 10.1086/507472

Wang, J.-W., Lai, S.-P., Eswaraiah, C., et al. 2017, ApJ, 849, 157, doi: 10.3847/1538-4357/aa937f

Wardle, J. F. C., & Kronberg, P. P. 1974, ApJ, 194, 249, doi: 10.1086/153240

Whittet, D. C. B. 1992, Dust in the galactic environment (Dust in the galactic environment Institute of Physics Publishing, 306 p.). http://adsabs.harvard.edu/cgi-bin/nph-bib_query?bibcode= 1992QB791.W45......&db_key=AST

—. 2003, Dust in the galactic environment - 2:nd ed. (Dust in the galactic environment Institute of Physics Publishing, 390 p.). http://adsabs.harvard.edu/cgi-bin/nph-bib_query?bibcode= 2003QB791.W45......&db_key=AST

Whittet, D. C. B., Gerakines, P. A., Hough, J. H., & Shenoy, S. S. 2001, ApJ, 547, 872, doi: 10.1086/318421

Whittet, D. C. B., Hough, J. H., Lazarian, A., & Hoang, T. 2008, ApJ, 674, 304, doi: 10.1086/525040

Whittet, D. C. B., Shenoy, S. S., Bergin, E. A., et al. 2007, ApJ, 655, 332, doi: 10.1086/509772

Whittet, D. C. B., & van Breda, I. G. 1978, A&A, 66, 57

Wilking, B. A., Lebofsky, M. J., Kemp, J. C., Martin, P. G., & Rieke, G. H. 1980, ApJ, 235, 905

Wright, C. O., Egan, M. P., Kraemer, K. E., & Price, S. D. 2003, AJ, 125, 359, doi: 10.1086/345511

Ysard, N., Abergel, A., Ristorcelli, I., et al. 2013, A&A, 559, A133, doi: 10.1051/0004-6361/201322066